RSC Advances

PAPER

View Article Online
View Journal | View Issue

Cite this: *RSC Adv.*, 2026, **16**, 21908

Syntheses, DNA interactions, and photodynamic antimicrobial properties of near-infrared indolium carbocyanine dyes

Carine P. Seudieu Seudieu,[a] Güliz Ersoy Özmen,†[a] Imran Khan,†[a] Maged Henary *[ab] and Kathryn B. Grant *[ab]

This study describes the design, syntheses, and evaluation of two new near-infrared (NIR) carbocyanine dyes as candidate photosensitizing agents for antimicrobial photodynamic therapy (aPDT). In aPDT, light activates photosensitizers to produce cytotoxic reactive oxygen species (ROS), to remediate treatment-resistant microbial infections. The carbocyanines feature terminal indolium groups connected by a heptamethine chain, enabling absorption of light in the tissue-penetrating NIR region. They also incorporate strategically positioned halogen atoms for improving hydrophobicity, chemical stability, and triplet-state yields. To enhance interactions with negatively charged bacterial cell walls and DNA, the dyes have different net charges at pH 7.0 (+1 *vs.* +2) and quaternary ammonium contents (QAC = 0 *vs.* 1). Across all experiments, the di-cationic carbocyanine (QAC = 1) outperformed its mono-cationic counterpart (QAC = 0), showing markedly greater stability in neutral aqueous solutions and generating higher levels of direct plasmid DNA strand breakage and hydroxyl radical/singlet oxygen ROS production under both 780 nm and broad-spectrum (707–759 nm) NIR irradiation. Spectral analyses and competitive binding assays indicated that monomeric and aggregated forms of the di-cationic carbocyanine bind within the minor groove of B-form DNA. At sub-micromolar concentrations, the di-cationic dye exhibited minimal dark toxicity toward cultured *E. coli* cells. However, upon 780 nm illumination, it was approximately tenfold more effective at inhibiting growth of this Gram-negative bacterium than its mono-cationic counterpart and the established aPDT agents indocyanine green and methylene blue (pH 7.0). These findings highlight the importance of developing di-cationic NIR carbocyanine dyes for aPDT applications.

Received 22nd February 2026
Accepted 17th April 2026

DOI: 10.1039/d6ra01566b

rsc.li/rsc-advances

1 Introduction

Bacteria cause infections that range in intensity from mild to life-threatening.[1] While the 20th century development of conventional antibiotics remains a groundbreaking medical advance, bacterial infectivity continues to have a major, negative impact on public health due to the phenomenon of antibiotic drug-resistance. When bacteria fail to respond to treatment, localized disease can become systemic, causing sepsis.[2]

A 2019 Institute for Health Metrics and Evaluation study of 204 countries and territories estimated that 23 bacterial pathogens caused ~4.95 million annual deaths that were related to antibiotic resistant bacteria.[3] The six most lethal pathogens included the four Gram-negative strains *Escherichia coli*, *Klebsiella pneumoniae*, *Acinetobacter baumannii*, and *Pseudomonas aeruginosa.* Compared to Gram-positive bacteria, Gram-negative pathogens are more prone to innate resistance to multiple antibiotics[4] due to the enhanced permeability barriers afforded by their complex cell wall structures.[5,6] There exists a great need for new therapeutic approaches to eradicate resistant bacterial infections.

Photodynamic therapy (PDT) is an up-and-coming strategy to treat diseases such as early-stage cancers and age-related macular degeneration.[7,8] The technique involves administering a non-toxic photosensitizer (PS) *via* topical, oral, or intravenous routes. The PS molecules in target tissues are then activated by light to form extremely short-lived and cytotoxic reactive oxygen species (ROS) that work exclusively at their sites of origin. This spatial and temporal control minimizes adverse side effects by selectively destroying cells in diseased tissues. The cytotoxic ROS generated during PDT arise from two primary mechanisms.[7,8] Initially, the PS is in its singlet ground state (S_0) and after absorbing light, transitions to a singlet excited-state S_1. Upon intersystem crossing, a lower-energy, longer-lived triplet state (T_1) is then reached. In the T_1 state, the PS can

[a]*Department of Chemistry, Georgia State University, Atlanta, Georgia 30302-3965, USA. E-mail: kbgrant@gsu.edu; mhenary1@gsu.edu*

[b]*Center for Diagnostics and Therapeutics, Georgia State University, Atlanta, Georgia 30303-5090, USA*

† These authors contributed equally to this work.

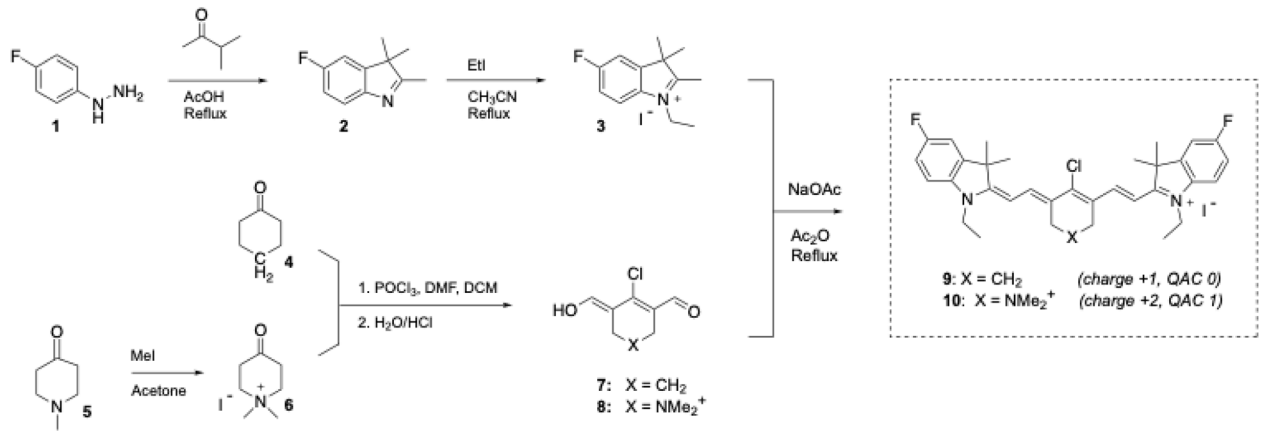

Scheme 1 Syntheses of heptamethine carbocyanine dyes **9** and **10**. Details regarding experimental and compound characterization can be found in the SI file accompanying this manuscript (Fig. S2 to S7). Abbreviations: charge = net charge at pH 7.0; QAC = quaternary ammonium content, excluding quaternary amines by resonance.

interact with ground state triplet oxygen ($^3O_2$) *via* type I electron transfer, giving rise to superoxide anion radicals ($O_2^{\bullet-}$). These radicals then undergo enzymatic or spontaneous dismutation to produce hydrogen peroxide (H_2O_2), which reacts with trace Fe^{2+} ions by the oxidative Fenton reaction to generate the strongly oxidizing hydroxyl radicals ($^\bullet$OH).[9,10] Alternatively, the T_1 state of the PS can undergo type II energy transfer to $^3O_2$ to form the ROS singlet oxygen ($^1O_2$). With respective diffusion distances of 0.8–6.0 nm[11] and 50–100 nm,[12] and half-lives of 1 ns[13] and 3 μs,[14] the highly reactive hydroxyl radicals and singlet oxygen vigorously oxidize nearby macromolecules – such as nucleic acids, proteins, and lipids. This multitargeted oxidative damage ultimately leads to cell death specifically in tissues exposed to light *via* apoptotic (programmed) and/or inflammatory/necrotic (non-programmed) mechanisms.[15]

Leveraging the same fundamental principle of highly localized, ROS-induced cellular damage, antimicrobial photodynamic therapy (aPDT) broadens PDT applications as a new tool to combat drug-resistant bacterial infections.[16] Unlike most antibiotics, aPDT does not rely on deactivating one or a few biochemical pathways or enzymes. Instead, the cytotoxic, short-lived ROS generated upon exposure of aPDT agents to light attack different types of molecules within and around targeted cells. Drug resistance therefore evolves at a reduced rate in aPDT as the microorganisms can no longer rely on a single genetic mutation or pathway change to survive.[4,6,17,18] Through its broad oxidative capabilities, aPDT works *in vivo* to resolve infections involving bacteria (*e.g.*, the extensively drug-resistant Gram-negative bacterium *Acinetobacter baumannii)*,[19] complex biofilms (*e.g.*, of the multidrug resistant Gram-negative bacterium *Pseudomonas aeruginosa*),[20] fungi[4,17] (*e.g.*, *Candida* spp.),[4] viruses,[4,17] and different microorganisms present at the same infection site.[17]

Among approved aPDT photosensitizers, good clinical outcomes have been often obtained with positively charged phenothiazine methylene blue (MB)[4,6,17,21–26] ($\lambda_{max,\ pH\ 7.0}$ = 664 nm) and other photosensitizers such as the negatively charged benzo[*e*]indolium heptamethine carbocyanine dye indocyanine green (ICG)[17,27–31] ($\lambda_{max,\ pH\ 7.0}$ = 669 to 778 nm), especially in the adjunctive treatment of bacterial periodontitis and root canal disinfections (Fig. S1 in SI). Industrial interest in aPDT is now growing, particularly in Europe and Canada. Anti-bacterial products currently on the market include the light-activated self-disinfecting surface coating Dyphox®,[24] various systems and kits used by dentists and at-home consumers to prevent and treat endodontic and periodontal infections (*e.g.*, MB-based Periowave™ and HELBO®; ICG-based Lumoral®; FotoSan® containing the phenothiazine Toluidine Blue O;[32–35] and Steriwave™,[36] a MB-based nasal photo disinfection system for the prevention of surgical site infections. Multiple MB[17,21–23,26,44–48] and ICG[22,34–38,48] aPDT clinical trials have been conducted or are currently in progress world-wide.

Although promising, aPDT photosensitizers targeting bacteria face challenges, which include limited cell wall penetration and/or poor transmission of the required photosensitizing irradiation through biological media.[6] In the present study, we have designed new aPDT photosensitizers that address these limitations. An ideal aPDT agent should be non-toxic in the dark, absorb 700 nm to 900 nm near-infrared (NIR) light to minimize the absorption of incident irradiation by surrounding biological tissues, and bear a net positive charge to facilitate its transport across the negatively charged cell walls characteristic of both Gram-positive and Gram-negative bacteria.[25]

Herein, we have developed and evaluated two symmetrical carbocyanine dyes as phototherapeutic antimicrobial agents (**9** and **10** in Scheme 1). Both are equipped with a heptamethine framework that red-shifts absorption into the NIR wavelength range and delocalizes a single positive charge between the two indolium rings of each dye. A second positive charge was incorporated into the heptamethine bridge of dye **10** *via* a cyclohexene quaternary ammonium group to promote interactions with the negative charge of DNA[37] and of bacterial cell walls.[38,39] The two NIR aPDT agents **9** and **10** thus differ with respect to net charge at pH 7.0 (+1 and +2) and quaternary ammonium content (QAC; 0 and 1). After characterizing DNA

interactions and photosensitized ROS generation, the two heptamethine carbocyanines were tested in under 780 nm NIR irradiation in phototoxicity assays against Gram negative *E. coli* cells. Bearing a net charge of +2, dye **10** was overwhelmingly superior to mono-cationic dye **9** and approximately 10 times more phototoxic to the *E. coli* than the conventional photosensitizing agents methylene blue and indocyanine green.

2 Experimental

2.1 General

All purchased reagents were of the highest available quality and were utilized without additional purification. Aqueous solutions were prepared with sterilized deionized distilled water. Agarose and deuterium oxide (99.9%) were respectively purchased from BioRad and Cambridge Isotope Laboratories. Bacto-agar, Bacto-tryptone, and Bacto-yeast extract were from Difco. Sodium benzoate (SigmaUltra, minimum 99%), methyl green, and pentamidine isethionate salt were provided by Sigma-Aldrich. Fluorescein was purchased from GTI Laboratory Supplies. XL1-Blue *E. coli* K-12 competent cells[40] and all other regents, including deferoxamine mesylate, dimethyl sulfoxide (DMSO, ≥99.99%), ethidium bromide, ethylenediaminetetraacetic acid (EDTA), hydroxyphenyl fluorescein (HPF), Singlet Oxygen Sensor Green (SOSG), Tiron (disodium 4,5 dihydroxy-1,3-benzenedisulfonate), and UltraPure calf thymus (CT) DNA (10 mg mL^{-1}, average size ≤2000 bp) were from ThermoFisher Scientific. The pUC19 plasmid was cloned using the Blue *E. coli* K-12 competent cell by standard methods[41] and was purified as with a QIAfilter Plasmid Mega Kit (Qiagen; Cat. No. 12263). Organic reactions were monitored using silica gel 60 F254 thin layer chromatography plates (Merck EMD Millipore, Darmstadt, Germany). ^{1}H NMR (400 MHz) and ^{13}C NMR (100 MHz) spectra were recorded on a Bruker Avance III spectrometer using either DMSO-d_6 (Cambridge Isotope Laboratories, Andover, MA), or $CDCl_3$ (Sigma-Aldrich, Burlington, MA) as solvent. High resolution electrospray ionization mass spectra (ESI-MS) were acquired for samples in 75% methanol with 0.1% of formic acid by the Georgia State University Mass Spectrometry Facility using a Xevo-G2-xs Q-TOF Mass Spectrometer (Waters Corporate, Milford, MA). HPF and SOSG emission were recorded on a SpectraMax iD5 Multi-Mode Microplate Reader (Molecular Devices, San Jose, CA, USA) using BrandTech black, flat-bottomed 96-well plates from Thomas Scientific (Cat. No. 1226J22). Circular dichroism spectra were measured with a Jasco J-1500 spectropolarimeter (Easton, MD, USA). UV-visible absorption and fluorescence emission spectra were respectively acquired using PerkinElmer Lambda 35 and LS55 spectrophotometers.

2.2 Cyanine dye syntheses

Known synthetic precursors **1** through **8** (Scheme 1) were either purchased commercially or prepared according to the published procedures described in SI.

2.2.1 2-((*E*)-2-((*E*)-2-Chloro-3-(2-((*E*)-1-ethyl-5-fluoro-3,3-dimethylindolin-2-ylidene)ethylidene)cyclohex-1-en-1-yl)vinyl)-1-ethyl-5-fluoro-3,3-dimethyl-3*H*-indol-1-ium iodide (9). The precursor 1-ethyl-5-fluoro-2,3,3-trimethyl-3*H*-indol-1-ium iodide (**3**) (500 mg, 1.5 mmol) and sodium acetate (369 mg, 4.5 mmol) were dissolved in acetic anhydride (10 mL). The reaction mixture was stirred at room temperature for 30 min. (*E*)-2-chloro-3-(hydroxymethylene) cyclohex-1-ene-1-carbaldehyde (**7**) (129.4 mg, 0.75 mmol) was then added to the solution and refluxed for 5 h. After excess solvent was removed with a rotovap, the reaction mixture was cooled down to room temperature, filtered, and subsequently washed with minimal amounts of ethanol, ethyl acetate and hexane. Product **9** was then purified by recrystallization using DMSO : EtOAc (5 : 95) and dried under a vacuum overnight. Yield: (0.21 g, green solid, 41%). MP > 288 °C, UV-vis (DMSO): λ_{max}/nm (ε/M^{-1} cm^{-1}) 791 (1.9164×10^5). ^{1}H NMR (400 MHz, $CDCl_3$): δ 8.31 ppm (d, J = 14.1 Hz, 2H), 7.22 (dd, J = 9.5, 3.7 Hz, 2H), 7.09 (t, J = 7.6 Hz, 4H), 6.14 (d, J = 14.1 Hz, 2H), 4.24 (q, J = 7.1 Hz, 4H), 2.70 (t, J = 6.0 Hz, 4H), 2.01–1.90 (m, 2H), 1.70 (s, 12H), 1.44 (t, J = 7.2 Hz, 6H). ^{13}C NMR (100 MHz, $CDCl_3$): δ ppm 171.72, 171.70, 162.11, 159.67, 150.62, 144.26, 143.10, 143.02, 137.78, 137.76, 127.41, 115.74, 115.50, 112.01, 111.93, 110.46, 110.21, 101.05, 49.52, 49.50, 40.47, 28.01, 26.71, 20.65, 12.43. ESI-MS (positive mode) calculated for $C_{34}H_{38}ClF_2N_2^+$: m/z 547.2692; found: m/z 547.2737.

2.2.2 2-((*E*)-2-((*E*)-4-Chloro-5-(2-((*E*)-1-ethyl-5-fluoro-3,3-dimethylindolin-2-ylidene)ethylidene)-1,1-dimethyl-1,2,5,6-tetrahydropyridin-1-ium-3-yl)vinyl)-1-ethyl-5-fluoro-3,3-dimethyl-3*H*-indol-1-ium iodide (10). Substituted indole **3** (500.0 mg, 1.5 mmol) and sodium acetate (184.6 mg, 2.2 mmol) were dissolved in acetic anhydride (10 mL). (*E*)-4-chloro-5-formyl-3-(hydroxymethylene)-1,1-dimethyl-1,2,3,6-tetrahydropyridin-1-ium (**8**) (246.9 mg, 0.75 mmol) was added to the solution which was then stirred at room temperature for 24 h. The solvent was removed with a rotovap and the product was purified using a short pad of silica gel with an eluent of 10% MeOH in DCM to give **10** as a green solid. Yield: (0.20 g, 32%). MP > 204 °C. UV-vis (DMSO): λ_{max}/nm (ε/M^{-1} cm^{-1}) 763 (2.1029×10^5). ^{1}H NMR (400 MHz, DMSO-d_6): δ ppm 8.21 (d, J = 14.6 Hz, 2H), 7.72 (d, J = 8.1 Hz, 2H), 7.64–7.56 (m, 2H), 7.35 (t, J = 8.9 Hz, 2H), 6.36 (d, J = 14.7 Hz, 2H), 4.78 (s, 4H), 4.37 (d, J = 6.9 Hz, 4H), 3.36 (s, 6H), 1.71 (s, 12H), 1.36 (t, J = 6.8 Hz, 6H). ^{13}C NMR (100 MHz, DMSO-d_6): δ ppm 174.48, 162.53, 160.11, 144.43, 144.34, 143.12, 143.08, 138.09, 116.13, 115.88, 114.05, 113.96, 113.69, 111.45, 111.20, 101.81, 60.50, 52.25, 50.33, 50.31, 27.53, 13.10. ESI-MS (positive mode) calculated for $C_{35}H_{42}ClF_2N_{32}^+$: m/z 288.6507; found: m/z 288.6508.

2.3 UV-visible absorption spectrophotometry

Time course absorption spectra were recorded at intervals of 0 up to 30 min. Cuvettes contained 10 μM of dye in neat CH_3CN (**9** or **10**), in neat DMSO (ICG or MB), or in 10 mM sodium phosphate pH 7.0 in the absence and presence of 150 μM bp CT DNA (500 μL final volume, 22 °C). Additional studies were carried out with the following adjustments. For Beer's Law plots, dye **9** and **10** spectra were recorded in DMSO for samples containing increasing 1.0×10^{-6} to 1.0×10^{-5} M or 1.0×10^{-6}

to 5.0×10^{-6} M of dye. Then the molar extinction coefficients at the λ_{max} of each dye were estimated by linear regression analysis. In DNA titration experiments, small volumes of CT DNA were sequentially added to samples containing 10 μM dye **10** in 10 mM sodium phosphate pH 7.0 with an initial volume of 500 μL and final volume of 550 μL to give CT DNA concentrations ranging from 27 μM bp up to 1223 μM bp. In competitive DNA binding studies, UV-visible spectra were recorded for 500 μL solutions of 10 mM sodium phosphate buffer pH 7.0 and one or more of the following: 10 μM of dye **10**, 250 μM of pentamidine, 250 μM of methyl green, and 150 μM bp CT DNA (22 °C).

2.4 DNA photocleavage

Reactions were run in 1.5 mL Eppendorf tubes containing 50 μM of dye **9** or **10** with 38 μM bp of pUC19 plasmid DNA and 10 mM of sodium phosphate (pH 7.0), for a total reaction volume of 40 μL. To control reaction temperature, a 38 × 25 × 6 cm glass baking dish (Pyrex) was filled with crushed ice. Then, an aluminum metal block was placed in the ice for about 5 min for the block to cool down to 10 °C. The reactions in the Eppendorf tubes were put into wells in the metal block which made tight contact with the entire external surface of each tube, leaving just the tube opening exposed. The samples in the ice-immersed block were either kept in the dark or irradiated for 30 min either with a 741 nm LED medical lamp (0.3 W cm^{-2}, spectral output 707–759 nm; Larson Electronics) or a monochromatic 780 nm LED laser (1.8 mW cm^{-2}; Techood). For the irradiated reactions, the Eppendorf tubes were left uncapped, and the LED medical lamp or laser was positioned 50 mm above the 10.8 mm diameter opening of each tube. Following irradiation, 3 μL of loading buffer containing 15.0% (w/v) ficoll and 0.025% (w/v) bromophenol blue were added to each sample. Twenty μL aliquots of the resulting solutions were loaded into the wells of 1.5% agarose gels containing ethidium bromide (EtBr) at a final concentration of 0.5 μg mL^{-1}. Electrophoresis was performed at 100 V for 60 min using a Bio-Rad Laboratories apparatus filled with 1X tris-acetate-EDTA (TAE) running buffer containing 0.5 μg mL^{-1} EtBr. After electrophoresis, gels were visualized under 302 nm light with a VWR Scientific LM-20E transilluminator and imaged with a UVP PhotoDoc-It™ system. DNA band intensities were quantitated using ImageJ software (National Institutes of Health). For supercoiled DNA, integrated intensity values were multiplied by a factor of 1.22 (ref. 42) to account for the increased affinity of ethidium bromide to the nicked and linear plasmid forms. DNA photocleavage yields were then calculated using the equation: percent photocleavage = [(linear + nicked DNA)/(linear + nicked + supercoiled DNA)] × 100.

Subsequent photocleavage reactions were conducted as just described, with adjustments. For dye titration experiments, the concentration of dye **10** was varied from 0 to 50 μM. The reactions mixtures in Eppendorf tubes were placed in a metal block immersed in a 10 °C ice bath and then shielded from light with aluminium foil or irradiated for 30 min with the 741 nm LED medical lamp.

2.5 Circular dichroism

CD samples contained 10 μM of dye **10** in 10 mM sodium phosphate pH 7.0 with and without 27 μM bp up to 1223 μM μM bp of CT DNA (final volume 2000 μL). Spectra were recorded at 22 °C from 200 to 900 nm using 3 mL quartz cuvettes (1.0 cm path-length; Starna). Instrument settings were: response and digital integration times, 4 s; scan rate, 100 nm min^{-1}; sensitivity, 200 millidegrees. Each final spectrum represents the average of at least 12 scans.

2.6 Fluorescence spectrometry

Solutions of 10 mM sodium phosphate buffer (pH 7.0), 0 or 10 μM of dye **10**, and CT DNA concentrations ranging from 0 μM bp up to 1223 μM bp were transferred to quartz cuvettes (2000 μL total volume). Fluorescence emission spectra were then acquired at λ_{ex} values of 680 nm, 740 nm, 760 nm, and 780 nm (22 °C). The scan speed of the fluorescence spectrophotometer was 100 nm min^{-1}, gain was set at medium, and the excitation and emission slit widths were both 4.5 nm.

In ROS detection experiments, fluorescence emission was measured for reactions containing 10 mM sodium phosphate buffer (pH 7.0) with or without 0.5 μM of dye **9** or **10** and either 3 μM of the hydroxyl radical probe hydroxyphenyl fluorescein (HPF)[43] or 1 μM of the singlet oxygen probe Singlet Oxygen Sensor Green (SOSG)[44] (final volume of 1500 μL).[45] Parallel HPF and SOSG reactions with chemical additive contained either 100 mM of sodium benzoate, 5 mM of deferoxamine mesylate, or 90% (v/v) of D_2O (1500 μL, final volume). Reactions were then irradiated with a 780 nm LED laser (1.8 mW cm^{-2}; Techood) and/or a 741 nm LED medical lamp (0.3 W cm^{-2}, spectral output 707–759 nm; Larson Electronics) or kept in dark (30 min, 22 °C) and transferred to a 96-well plate (total volume per well, 200 μL). Fluorescein standards of 75 nM and 350 nM in 10 mM NaOH were respectively used for HPF and SOSG reactions (200 μL per well). HPF and SOSG emission was recorded with the λ_{ex}/λ_{em} wavelengths set at 490/525 nm using a SpectraMax iD5 Multi-Mode Microplate Reader then averaged over two to four independent trials with error bars indicating standard deviation.

2.7 Reagent-induced changes in DNA photocleavage

Solutions containing 10 mM of sodium phosphate buffer (pH 7.0) and 38 μM bp of pUC19 plasmid DNA were prepared with or without 30 μM of dye **10** and a chemical additive, either 100 mM of sodium benzoate, 100 mM of EDTA, 10 mM of Tiron, or 79% D_2O (v/v), in a final volume of 40 μL. The reactions were then irradiated for 30 min with the 741 nm LED medical lamp (0.3 W cm^{-2}) or kept in the dark (22 °C). Following irradiation, DNA photocleavage products were separated on 1.5% non-denaturing agarose gels, visualized, and quantitated as just described. The percent inhibition of DNA photocleavage caused by each chemical additive was calculated using the equation: percent inhibition = [((%linear + %nicked DNA with additive) − (%linear + %nicked DNA without additive))/(%linear + %nicked DNA without additive)] × 100.

2.8 Phototoxicity assay

All solutions, media, and plasticware were autoclaved prior to use. Starter cultures of XL1-Blue *E. coli* K-12 competent cells (5 mL) were grown at 37 °C for 8 h in Luria-Bertani (LB) broth under vigorous shaking. An aliquot of the starter culture (~5 μL) was then transferred to fresh LB broth to obtain 5 mL of a bacterial suspension with an optical density at 600 nm (OD_{600}) between 0.002 to 0.003. For photosensitization, 30 μL of ddH_2O, 4 μL of 100 mM sodium phosphate pH 7.0, 4 μL of the bacterial suspension, and 2 μL of dye stock solution (**9** or **10** in CH_3CN; MB or ICG in DMSO) were added to Eppendorf tubes to yield 40 μL reactions containing final concentrations of 0 to 32 μM of dye **9**, 0 to 0.6 μM of dye **10**, and 0 to 50 μM of MB or ICG. For controls without dye, 2 μL of solvent were used to substitute for ddH_2O. After a 5 min equilibration, samples were either irradiated with the monochromatic Techood 780 nm, 1.8 W cm^{-2} LED laser (dyes **9**, **10**, ICG), a monochromatic Laserlands 638 nm 2.8 W cm^{-2} LED laser (MB), or kept in the dark (30 min, 22 °C). After treatment, the 40 μL solutions were evenly spread on LB agar plates with an inoculating loop, incubated in the dark at 37 °C for 16 h, and then imaged. The colony numbers on each plate were quantified using ImageJ software. Cell viability for each plate was determined using the equation: (number of colonies on plate with dye/number of colonies on control plate without dye) × 100. The results were averaged over three independent experiments, with error bars indicating standard deviation.

3 Results and discussion

3.1 Design of aPDT agents

NIR carbocyanine dyes that effectively produce ROS are mainly used for photodynamic therapy.[46] Among them, indocyanine green (Fig. S1) is the most extensively studied cyanine photosensitizer in human clinical PDT trials, particularly for the treatment of periodontitis and other dental infections.[22,34–38,48] Often modified with heavy atoms (I, Br, Se) to optimize ROS yields,[47–49] some promising cyanine derivatives are under development, but have not yet advanced to human clinical evaluation. In an emerging application beyond medicine, NIR ROS-generating cyanine dyes are being developed as photocatalysts in organic synthesis.[50]

As exemplified by ICG and compounds **9** and **10** (Scheme 1), carbocyanine dyes are composed of two nitrogen-containing heterocyclic aromatic rings connected by a polymethine chain that delocalizes a single positive charge between them. The advantages of carbocyanines include minimal dark toxicity and excellent optical properties, including high molar absorption coefficients and strong fluorescence quantum yields, depending on the dye.[46,51] In addition, the absorption and emission maxima of carbocyanines can be easily red-shifted by modifying the terminal heterocyclic groups and/or by lengthening the connecting bridge. In the case of carbocyanines **9**, **10**, and ICG, their extended heptamethine conjugation brings dye absorption into the desired NIR wavelength range (Fig. 1 and S8). Thus, the deep tissue penetrating ability of the low energy photons required to activate heptamethine carbocyanines[52] renders these chromophores as highly promising PDT agents.[46] In addition to aPDT, indocyanine green is in extensive clinical use as a fluorescent probe in a variety of biomedical imaging applications.[51] However, ICG bears a net negative charge under physiological conditions, which could place limits on its effectiveness in aPDT treatment of infections caused by bacteria and other microorganisms encased by negatively charged cell walls (*e.g.*, most fungi and yeast).[53,54]

A number of steps were taken to design carbocyanine dyes **9** and **10** as aPDT-optimized photosensitizing agents (Scheme 1). We placed an electron withdrawing chlorine atom at the *meso* position of the heptamethine π-bridge of each dye. This was done to reduce spontaneous dye autooxidation (no *hν*),[55,56] and through a heavy atom effect, to increase intersystem crossing rates to the dyes' triplet excited states.[57] Rigidifying rings (either cyclohexene or tetrahydro-pyridinium) were incorporated into the bridges of carbocyanines **9** and **10**, respectively. This was implemented to further red-shift chromophore absorption by increasing planarity and to suppress non-radiative decay pathways that shorten excited triplet state lifetimes.[58] Our rationale for adding a fluorine atom onto each indolium ring of carbocyanines **9** and **10** was to promote dye interactions with the phospholipid bilayers present in bacterial cell walls. Replacing aromatic C–H with C–F bonds is a widely used strategy to increase the membrane permeabilities and hydrophobic targeting binding abilities of marketed drugs.[59,60] Examples include the cardiovascular agent Lipitor, the antidepressant Flunarizine, and fluoroquinolone antibacterial agents such as Ciprofloxacin, Levofloxacin, and Moxifloxacin, where fluorination enhances the drugs' passage through bacterial cell walls.[61] Fluorine is a weak hydrogen-bond acceptor that cannot increase water solubility by hydrogen bonding.[61] Moreover, its high electronegativity holds onto electrons more tightly than hydrogen, making the C–F bond poorly polarizable relative C–H and less able to engage in favourable electrostatic/induction interactions with water.[61] This leads to the stronger hydrophobic character of aromatic C–F bonds and increased drug lipophilicity compared to more polarizable C–H environments. Finally, to enhance interactions with negatively charged bacterial cell walls[38,39] and DNA,[37] we introduced a positively charged quaternary amino group into dye **10** *via* the cyclohexene ring of the linker, leaving dyes **9** and **10** with respective net charges of +1, and +2 (pH 7.0). Long used in antiseptics and disinfectants, cell wall-solubilizing quaternary ammonium groups are now being incorporated into existing antibiotics to afford next-generation antimicrobial agents with superior activities against resistant bacteria.[62,63] While quaternary ammonium salts are not uniquely selective, they show a distinct preference for bacterial cells over eukaryotic cells, when present at low concentrations.[39]

3.2 Chromophore stability and DNA interactions in solution

UV-visible absorption spectra recorded as a function of time indicate that heptamethine carbocyanine dyes **9** and **10** are stable in acetonitrile over 30 min (Fig. 1a and e). The frozen

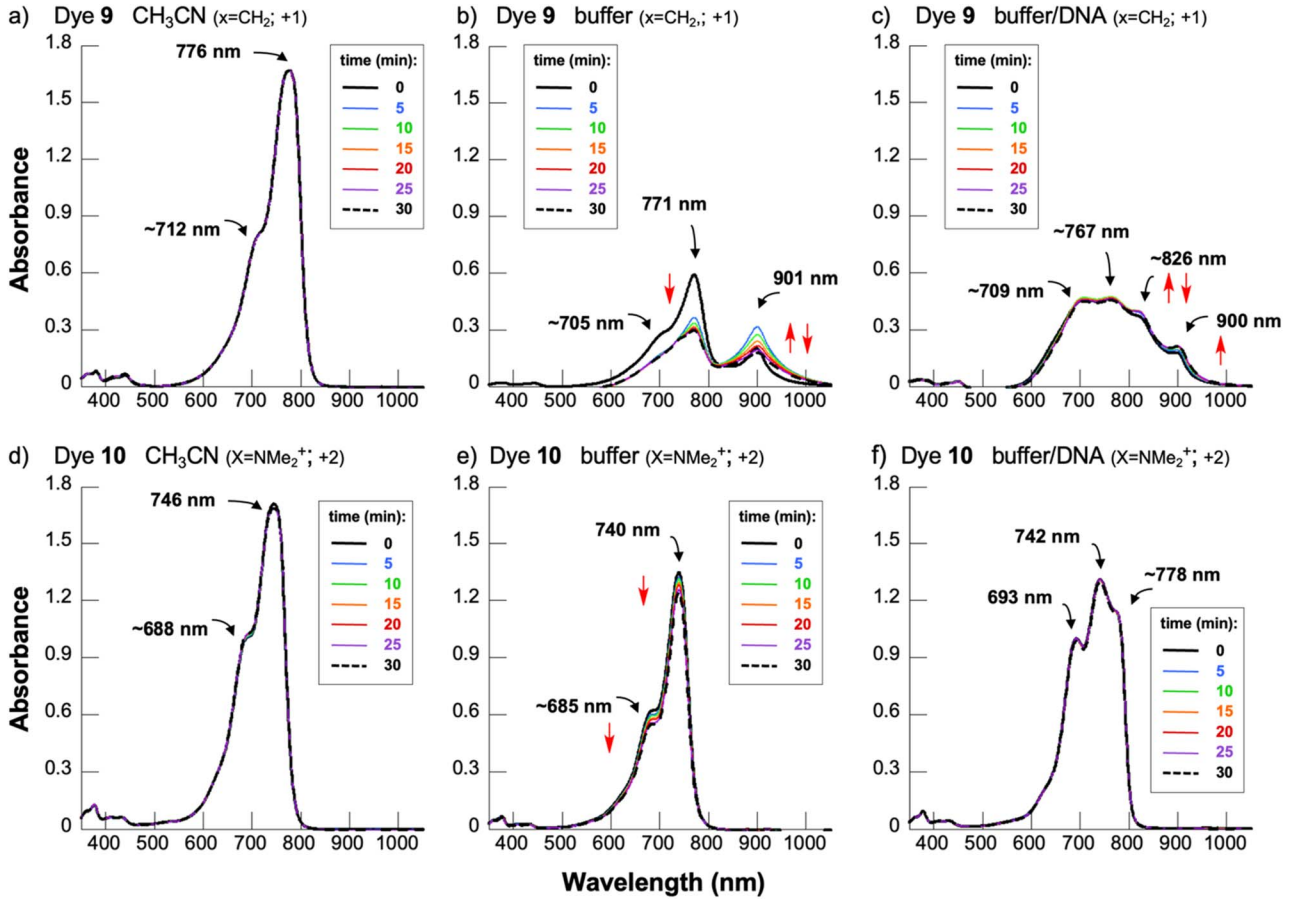

Fig. 1 UV-visible spectra recorded over 30 min for 10 μM of cyanine dyes **9** and **10** in: (a) and (d) neat acetonitrile; (b) and (e) 10 mM sodium phosphate buffer pH 7.0; (c) and (f) 10 mM sodium phosphate buffer pH 7.0 and 150 μM bp CT DNA (22 °C).

solutions of the dyes remained unchanged over months, leading us to use CH_3CN as a dye storage solvent (−20 °C, no *hν*). The absorption bands of dyes **9** and **10** in acetonitrile are all well-defined, with NIR λ_{max} values of 776 nm (dye **9**) and 746 nm (dye **10**) accompanied by respective high energy shoulders at ~712 nm and ~688 nm (Fig. 1a and d).

To test for hypsochromic H-type dye aggregation, DMSO solutions containing 1.0, 2.0, 3.0, 4.0, 5.0 and 10.0 μM of dyes **9** and **10** were read for absorption. (While DMSO was not optimal for stable, long-term storage of the dyes, it was used in place of acetonitrile in these experiments to avoid error caused by the high vapor pressure of the latter solvent (~88 mm Hg at 20 °C) leading to noticeable evaporation of CH_3CN from our 500 μL cuvettes.) We then employed the λ_{max} absorbance values at each dye concentration to plot the Beer's Law graphs in Fig. S9 of SI. The data show that carbocyanines **9** and **10** slightly deviate from linearity at 10.0 μM of dye due to a decrease in λ_{max} absorbance, particularly in the case of **10** (Fig. S9b and d). Upon carrying out a similar Beer's law analysis of dye **10**'s high energy shoulder (~705 nm in DMSO, Fig S9e), there was a corresponding 10.0 μM absorbance increase (Fig. S9d *vs.* e). We then charted the ratios obtained by dividing the absorbance at each dye's λ_{max} value by corresponding high energy shoulder absorbance (DMSO; Fig. S10). The results illustrate that the amounts of light taken up by dye **9** or **10** are diminished at the λ_{max} and enhanced at the hypochromic shoulder as a function of increasing dye concentration, a trend suggestive of the conversion of monomeric to aggregated dye forms. Polar aprotic solvents such as acetonitrile[64,65] and DMSO[66,67] possess much weaker hydrophobic driving forces than water and therefore do not strongly promote the aggregation of amphiphilic/hydrophobic solutes. As a result, it is conceivable that the main absorption bands of dyes **9** and **10** in CH_3CN and DMSO arise from monomeric dye while the hypsochromic shoulders correspond to H-type aggregates.[68] There is also a possibility that this putative aggregate absorption overlaps with hypsochromic, main peak vibrational fine structure, an optical feature in common to many carbocyanine dyes.[69] Highly linear spectral responses were seen when we excluded the 10 μM data points, to generate new λ_{max} Beer's Law plots from 1.0 up to 5 μM of each dye (Fig. S11b and d). The slopes of the resulting best straight-line fits were employed to estimate dye molar extinction coefficients in DMSO: dye **9**, $\varepsilon_{\lambda max} = 1.9164 \times 10^5\ M^{-1}\ cm^{-1}$ (λ_{max} = 791 nm); dye **10**, $\varepsilon_{\lambda max} = 2.1029 \times 10^5\ M^{-1}\ cm^{-1}$, ($\lambda_{max}$ = 763 nm).

The chemical and optical properties of carbocyanine dyes **9** and **10** in aqueous solutions were studied next. The peak absorption wavelengths and shoulders of the dyes in sodium

phosphate buffer (pH 7) were blue-shifted by ~3 nm to 7 nm with respect to neat acetonitrile (Fig. 1b and e *vs.* a and d). While both showed some signs of degradation in H_2O, the effect was more pronounced in the case of dye **9**, where the putative dye monomer was converted to a highly unstable, red-shifted species (λ_{max} = 901 nm; Fig. 1b). The main absorption band of dye **10** in neutral aqueous buffer, CH_3CN, and DMSO has a very similar shape, bandwidth, and high energy shoulder, indicating that the monomeric form of the dye and blue-shifted H-type aggregate might also exist in pH 7.0 buffered water (Fig. 1d, e and S9c).

Carbocyanine aromaticity and delocalized positive charge often enhance the ability of these dyes to bind to double-helical DNA in their monomeric and/or aggregated forms. Depending on binding mode, the aromatic rings of the monomers can either intercalate between DNA base pairs or, for both monomers and aggregates, form extensive van der Waals contacts with the walls of the B-form minor groove.[68,70,71] When we transferred genomic calf thymus (CT) DNA to our aqueous pH 7.0 buffered dye solutions, nucleic acid interactions were clearly indicated (Fig. 1c and f *vs.* b and e). The positions and of main spectral bands of dyes **9** and **10** were respectively blue- and red-shifted upon DNA addition, the dyes' high energy shoulders were red-shifted, and one or more bathochromic shoulders suggestive of possible J-type dye aggregation[68,71] were formed.

3.3 Carbocyanine dye-photosensitized ROS production

3.3.1 DNA photocleavage. Select classical antibiotics, including some fluoroquinolones (*e.g.*, norfloxacin), β-lactams (*e.g.,* ampicillin) and aminoglycosides (*e.g.*, kanamycin), trigger metabolic shifts that amplify ROS production.[72–74] Although the ROS are not the main mechanism for killing bacterial,[75] the damage to bacterial DNA caused by the ROS increase has been proposed to play a contributing, secondary role.[72–74] This being said, photosensitization reactions are known to generate ROS that cause significant DNA damage in the form of DNA adducts and/or direct strand breaks.[76]

To test carbocyanine dyes **9** and **10** for ROS activity, neutral aqueous solutions of *E. coli* plasmid DNA in the absence and presence of dye were either kept in the dark or irradiated for 30 min with a light source overlapping dye absorption: a broad spectrum 741 nm LED medical lamp (spectral output 707 nm to 759 nm) or a monochromatic 780 nm LED laser (Fig. 2). The reactions were then electrophoresed on non-denaturing agarose gels.[41] A change in the conformation of the plasmid from a compact, rapidly migrating supercoiled state to less mobile, nicked and linear DNA forms revealed photosensitized direct strand breakage of the DNA by both carbocyanine dyes (Fig. 2). Minimal levels of cleavage appeared in reactions without dye and/or irradiation. Under the 741 and 780 nm light sources, dye **10**, with a net charge = +2, was significantly more reactive towards the negatively charged DNA than mono-cationic dye **9**. Our findings complement a number of published studies in which polymethine carbocyanine dyes[49,67,77,78] and asymmetrical cyanines[79] photosensitize the production of DNA cleaving ROS in the visible or near-infrared wavelength range. The DNA photocleavage yields in our experiments likely reflect a combination of factors including dye stability, the molar absorptivity of each DNA/dye complex *vs.* lamp spectral output, and DNA/dye binding affinity.

DNA cleavage levels at dye **10** concentrations ranging from 2.5 μM up to 50 μM were examined next (741 nm *hν*, 30 min, pH

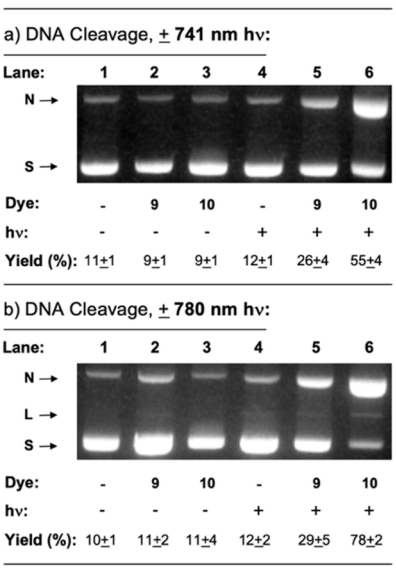

Fig. 2 Representative ethidium bromide-stained agarose gels depicting photocleavage of 38 μM bp pUC19 plasmid DNA in absence and presence of 50 μM of dyes **9** and **10** (10 mM sodium phosphate buffer pH 7.0). To prevent interference from heat arising from the LED lamps, the reactions were left in a ~10 °C metal block either: in the dark (−), or while being irradiated (+) for 30 min with (a) a 741 nm LED medical lamp or (b) a 780 nm, 1.8 mW cm^{-2} LED laser. Abbreviations: N, nicked; L, linear; S, supercoiled. Yields were averaged over 2 to 3 trials. Error bars show standard deviation.

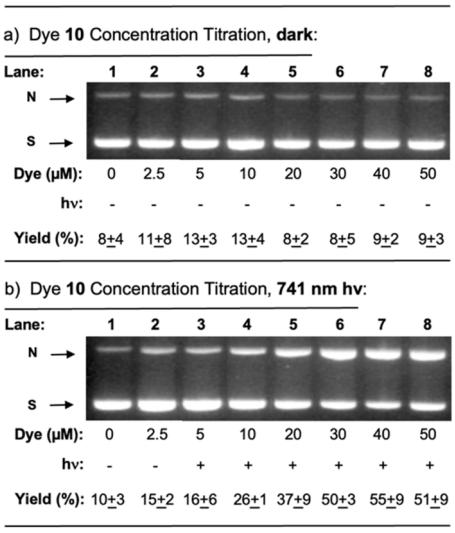

Fig. 3 Representative agarose gels showing photocleavage of 38 μM bp pUC19 DNA in the presence of dye **10** concentrations ranging from 0–50 μM (10 mM sodium phosphate buffer pH 7.0; 10 °C). Reactions were either (a) kept in the dark, or (b) irradiated with a 741 nm LED lamp (0.3 W cm^{-2}; spectral output 707–759 nm) for 30 min. Errors represent standard deviation. Abbreviations: N, nicked; S, supercoiled.

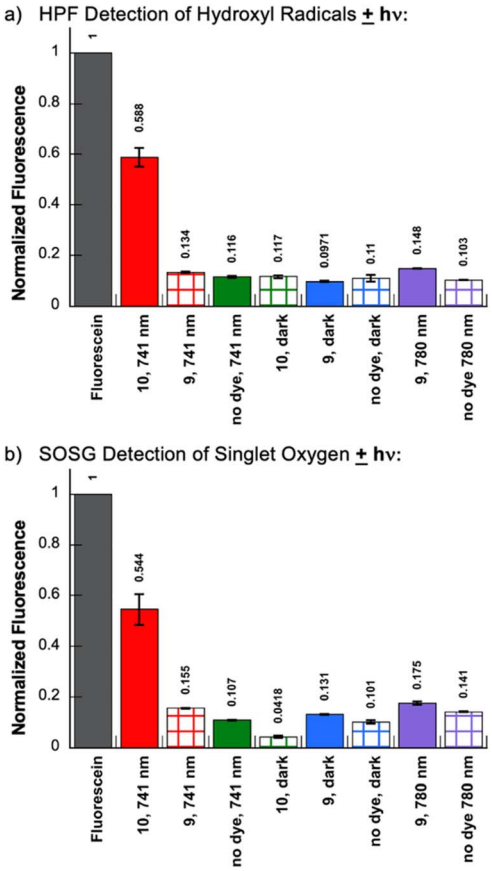

Fig. 4 Fluorescence emission of ROS probes. Reactions containing 10 mM sodium phosphate buffer (pH 7.0) in the presence and absence of 0.5 μM of dyes **9** and **10** and either (a) 3 μM of HPF or (b) 1 μM of SOSG, were either kept in dark or irradiated using the 780 nm, 1.8 mW cm^{-2} LED laser and/or a 741 nm, 0.3 W cm^{-2} LED medical lamp (30 min, 22 °C, no DNA). HPF (a) and SOSG (b) emission was recorded at 525 nm upon 490 nm excitation, normalized relative to respective 75 nM and 350 nM fluorescein standards, and averaged over 3 trials. Error bars represent standard deviation.

7.0; Fig. 3). As expected, photosensitized direct strand breakage generally increased with the amount of dye present in the reactions. Statistically significant levels of DNA photocleavage appeared at 10 μM of dye **10**, reaching a plateau at 30 μM to 50 μM of dye.

3.3.2 Identification of dye-photosensitized ROS. Potential ROS include superoxide anions radicals ($O_2^{\bullet -}$), hydrogen peroxide (H_2O_2), hydroxyl radicals ($^{\bullet}OH$), and singlet oxygen ($^1O_2$), but only $^{\bullet}OH$ and $^1O_2$ are reactive enough to directly break DNA.[80,81] To test for hydroxyl radical and singlet oxygen production by carbocyanine dyes **9** and **10**, we respectively employed the fluorescent probes hydroxyphenyl fluorescein (HPF) and Singlet Oxygen Sensor Green (SOSG).[45] Samples containing sodium phosphate buffer (pH 7.0) and HPF or SOSG, in the absence and presence of carbocyanine dyes **9** or **10**, were either kept in the dark or irradiated at 780 nm and/or 741 nm (30 min, 22 °C). DNA was not included due to the ability of nucleic acids to rapidly scavenge $^{\bullet}OH$ and $^1O_2$.[76] After the irradiation interval, the HPF and SOSG samples were loaded into the wells of a microplate and read for fluorescence with a microplate reader (Fig. 4). Significant levels of $^{\bullet}OH$ and $^1O_2$ were detected by the probes in the reactions containing dye **10** (net charge = +2). It is therefore possible that hydroxyl radicals and/or singlet oxygen contribute to the relatively high DNA cleavage levels photosensitized by this dye (Fig. 2). On the other hand, reactions with dye **9** (net charge = +1) gave rise to only slightly more fluorescence than irradiated control reactions without dye, even when the 0.3 W cm^{-2} 741 nm broad spectrum medical lamp was replaced with the more powerful 1.8 mW cm^{-2} 780 nm monochromatic laser (Fig. 4). Due to the instability exhibited by dye **9** in pH 7.0 buffered water (Fig. 1b), and the low levels of DNA photocleavage (Fig. 2) and DNA cleaving ROS (Fig. 4) photosensitized by this dye, most of the remaining studies in this paper are on focussed on carbocyanine **10**.

While SOSG is highly specific for $^1O_2$,[44] the popular hydroxyl radical probe HFP detects ($^{\bullet}OH$), peroxynitrite anions ($ONOO^-$), superoxide anions radicals ($O_2^{\bullet -}$), hypochlorite anions (ClO^-), singlet oxygen ($^1O_2$), and hydrogen peroxide (H_2O_2) at ratios of 730 (for $^{\bullet}OH$): 120 (for $ONOO^-$): 8 (for $O_2^{\bullet -}$): 6 (for ClO^-): 5 (for $^1O_2$): 2 (for H_2O_2).[43] To confirm the specificities of SOSG and HPF for the respective analytes $^1O_2$ and $^{\bullet}OH$, we next included the following chemical additives in cyanine dye **10** reactions: sodium benzoate, which scavenges hydroxyl radicals at near diffusion-controlled rates,[82] the Fe^{3+} chelator deferoxamine mesylate (DFM), which would reduce the formation of hydroxyl radicals arising from Fenton Chemistry,[9,10] and deuterium oxide, a solvent that extends the half-life of singlet oxygen by a factor of 10.[83] Upon irradiating dye **10**, both sodium benzoate and DFM significantly decrease the HPF signal while D_2O enhances SOSG fluorescence, thus supporting the respective detection hydroxyl radicals and singlet oxygen by the HPF and SOSG probes (Fig. 5).

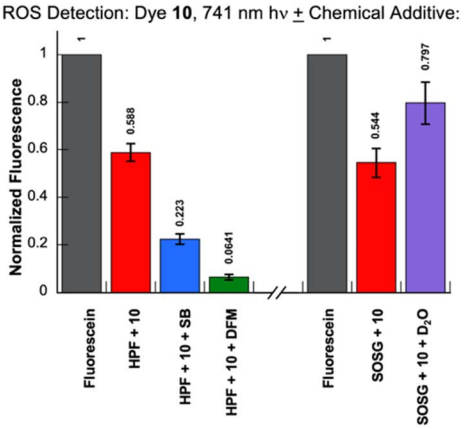

Fig. 5 Samples contained 10 mM sodium phosphate buffer pH 7.0, 3 μM HPF or 1 μM SOSG, 0.5 μM dye **10** in the absence and presence of a final concentration of: 100 mM of sodium benzoate, 5 mM of DFM, and 90% D_2O (v/v). The reactions were irradiated for 30 min using a 741 nm, 0.3 W cm^{-2} LED lamp (22 °C, no DNA). HPF and SOSG emission at 525 nm was recorded upon 490 nm excitation. Error bars represent standard deviation. HPF (left) and SOSG (right) emission data were normalized relative to respective 75 nM and 350 nM fluorescein standards and were averaged over 2 to 4 trials. Error is reported as standard deviation.

Table 1 DNA photocleavage upon additive addition[a]

Reagents added	Species targeted	Decrease in DNA direct strand breaks (%)
Na^+benzoate	$^{\bullet}OH$	77 ± 3
EDTA	M^{n+}	81 ± 3
Tiron	$O_2^{\bullet -}$	59 ± 8
D_2O	$^1O_2$	4 ± 5

[a] To reactions containing 10 mM sodium phosphate buffer pH 7.0, 38 μM bp of pUC19 plasmid DNA, and 30 μM of dye **10**, a final concentration of one of the following chemicals was added: sodium benzoate (100 mM), EDTA (100 mM), Tiron (10 mM), or 79% D_2O (v/v). The samples were kept in dark or were irradiated for 30 min alongside controls without additive using a 741 nm LED lamp (0.3 W cm^{-2}; 22 °C). Cleavage inhibition yields were averaged over 3 trials with error reported as standard deviation. A representative gel appears in Fig. S12 of SI.

3.3.3 DNA photocleavage mechanisms. To establish a link between hydroxyl radicals, singlet oxygen, and the DNA strand breakage (Fig. 2), reactions containing dye **10** and pUC19 plasmid DNA in the absence and presence of chemical additives were irradiated and then resolved on agarose gels. In addition to sodium benzoate and deuterium oxide, we employed the metal chelating agent EDTA, and Tiron to scavenge the hydroxyl radical precursor superoxide.[84] The percent of DNA photocleavage inhibition caused by each additive was calculated after integrating gel photographs (Table 1). The resulting data show that sodium benzoate, EDTA, and Tiron significantly reduce the formation of dye **10**-photosensitized DNA direct strand breaks, while replacing water with 79% D_2O (v/v) has a negligible effect (Table 1 and Fig. S12 in SI). Taken together with the HPF experiments in Fig. 4a and 5, these results suggest that hydroxyl radicals generated through metal-assisted Fenton chemistry contribute to DNA photocleavage by dye **10** (Fig. 2, 3, and S12).[9,85] Hydroxyl radicals vigorously cut the DNA backbone by abstracting hydrogen atoms from 2-deoxyribose.[85] In contrast, singlet oxygen mostly generates 8-hydroxy-2′-deoxyguanosine lesions (8-OHdG),[86] accompanied by small amounts of direct strand breakage.[87,88] The oxidized DNA adduct 8-OHdG requires alkaline conditions for DNA cleavage,[89] and therefore cannot be detected by non-denaturing agarose gel electrophoresis.

Redox active metal ions that fuel Fenton Chemistry are commonly found in trace amounts in purified plasmid DNA and in laboratory reagents including distilled water (*e.g.*, metals transferred from plasticware, equipment and the fumes and aerosols in ambient air).[90,91] Adventitious levels of weakly chelated, redox active iron and copper ions are also present in living organisms under conditions of oxidative stress,[92,93] where they play a major role in accelerating cellular damage and death through rapid Fenton-driven hydroxyl radical production.[94–96]

3.4 DNA binding mode analyses

3.4.1 UV-visible spectrophotometry. Absorption spectra of dye **10** in pH 7.0 buffered ddH_2O were sequentially recorded upon CT DNA addition (Fig. 6). As the DNA concentration of the solution was gradually increased, the dye's main peak was red-shifted from 740 nm to 746 nm and then gained intensity, confirming dye/DNA binding interactions. The final, main 746 nm dye absorption band at 1223 μM bp of DNA (solid black line in Fig. 6), is very similar in shape to the main absorption band of free dye in the buffer (dashed black line in Fig. 6, λ_{max} = 740 nm), CH_3CN (Fig. 1d, λ_{max} = 746 nm), and DMSO (Fig. S9c, λ_{max} = 763 nm), suggesting that the dye is interacting with DNA in its monomeric form. The high energy shoulder between ~685–693 nm, a putative H-type aggregate (Fig. 1f), lost absorption upon DNA addition. At the same time, a red-shifted shoulder between ~785–780 nm emerged, then gradually subsided as the titration was continued, confirming possible J-type aggregation of cyanine dye **10** (Fig. 1f).[71] While B-form DNA serves as a template for dye aggregation, raising DNA concentrations above threshold levels "solubilizes" H-[70] and J-[71] cyanine aggregates to re-form monomeric dye and lower order aggregates. Initial UV-visible spectra containing the DNA likely represent the absorption of free and bound dye, with the equilibrium gradually shifting towards the DNA-bound state as more nucleic acid is added. The titration experiment was stopped after the added volume of concentrated DNA exceeded 10%[97] of the initial 500 μL solution volume to avoid disrupting binding equilibria. As a results, a titration endpoint could not be reached (Fig. 6).

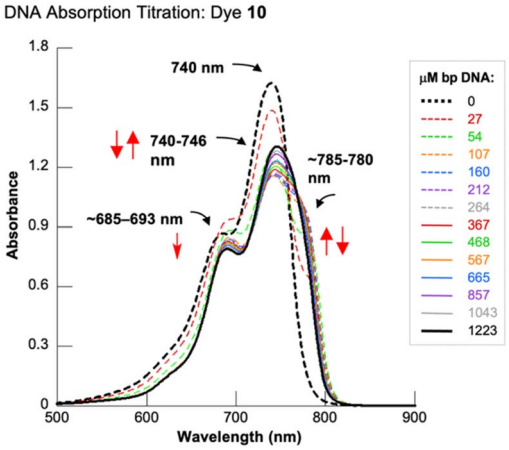

Fig. 6 UV-visible absorption spectra of solutions containing 10 μM of dye **10**, 10 mM sodium phosphate buffer pH 7.0 in the absence and presence of increasing CT DNA concentrations from 27 μM bp up to 1223 μM bp (22 °C).

3.4.2 Circular dichroism. Binding interactions between chiral B-form DNA and achiral ligands generate induced circular dichroism (ICD) signals that give valuable insights into ligand DNA binding modes. For example, the ICDs of DNA intercalators are relatively weak and have signs that are either positive or negative when the orientation of the dye's transition moment relative to the pseudo dyad axis of the DNA duplex is either parallel or perpendicular, respectively.[98] Monomeric and dimeric ligands that bind to the DNA minor groove are typically associated with strong positive ICD signals.[68,98] Upon forming end-to-end dimers and higher order aggregates, most DNA ligands bind either externally[99] or in the DNA minor

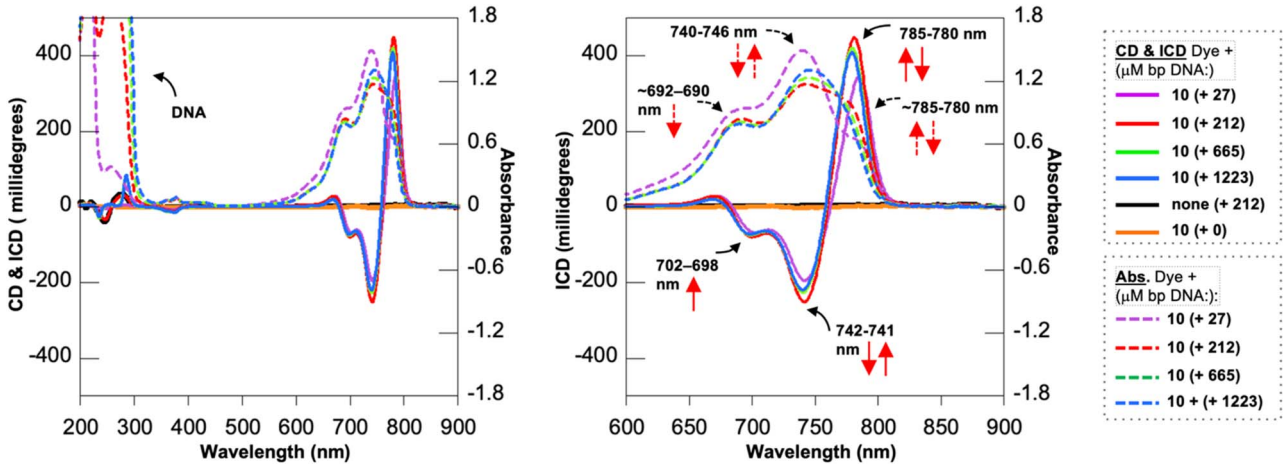

Fig. 7 Double *y*-axis plots superimposing the circular dichroism (CD) and/or induced circular dichroism (ICD) spectra and corresponding UV-visible absorption (Abs.) spectra. Data were recorded for samples containing 10 mM sodium phosphate buffer pH 7.0 in the absence and presence of 10 μM of dye 10 and CT DNA concentrations ranging from 0 μM bp up to 1223 μM bp (22 °C). Absorption, CD & ICD spectra are plotted from 200 nm to 900 nm (left panel); absorption & ICD spectra are plotted from: 600 to 900 nm (right panel). The absorption spectra were taken from Fig. 6.

grooves.[68,70,71] This aggregate formation typically generates a strong, signature exciton coupling ICD signal that when compared to the absorption spectrum of the aggregate can be used to determine not only aggregate handedness but H *vs.* J character.[100–103] In the case of cyanine H aggregates bound to right-handed B-form DNA, the main absorption band of the aggregate is usually blue-shifted relative to the dye monomer and sits near the high energy, negative lobe of the bisignate ICD couplet.[101] When staggered J aggregates interact with B-form DNA, the ordering is usually reversed. The aggregate's main absorption band is red-shifted relative to the monomer and overlaps with the low energy, positive couplet lobe.[100–103] The negative high-energy, positive low-energy lobe patterns of H and J aggregates bound to B-form DNA generally point to right handed exciton geometry consistent with the right handed B-form helix.[71]

We next recorded circular dichroism spectra of cyanine dye **10** in the absence and presence of increasing CT DNA concentrations. The ICD signals generated by binding of the achiral dye to the chiral DNA were then superimposed on corresponding dye absorption on double *Y* axis plots (Fig. 7). As expected, no CD signal was seen for achiral dye **10**. However, when DNA was introduced, the titration data revealed a strong bisignate exciton coupling ICD signal consistent with right-handed J-aggregation templated by right-handed B-form DNA.[71] The bisignate feature is comprised of a negative 742–741 nm short wavelength lobe followed by a positive 785–780 nm long wavelength component that overlaps the DNA-induced, ~785–780 nm long wavelength shoulder in the absorption spectra of dye **10** (Fig. 7). Upon the sequential DNA addition, the positive ICD peak exhibits intensity changes (solid arrows in Fig. 7) like those seen in the long wavelength absorption shoulder (dashed arrows). Compared to the positive 785–780 nm bisignate ICD component, the negative 742–741 nm exciton peak is less intense, a spectral feature in common to many[100,102,103] but not all[71] DNA bound cyanine J-aggregates. The attenuated intensity and 702–692 nm shoulder of the negative ICD exciton Iobe might also be related to underlying, masked, positive ICD signals generated by competing DNA binding modes[104] (*e.g.*, the putative 692–690 nm H-aggregated and 740–746 monomeric forms of dye **10**; Fig. 7).

3.4.3 Fluorescence spectroscopy. Strong enhancements in fluorescence are commonly observed when cyanine monomers intercalate in between DNA base pairs. Conformational twisting is highly restricted by this binding mode, preventing non-radiative decay from the dye's singlet excited state and increasing fluorescence quantum yields.[68] In contrast, emission tends to be weaker when cyanine monomers bind in the DNA minor groove,[105] and is usually quenched upon the formation of groove-bound H-aggregates.[78,106] To re-screen for intercalative DNA binding by the monomeric form of dye **10**, fluorescence spectroscopy was employed.

Emission spectra of carbocyanine dye **10** were recorded in the presence of 0, 106, 567, 1042, and 1223 μM bp of CT DNA (pH 7.0; Fig. S13). The samples were excited at 680, 740, 760 and 780 nm, wavelengths strongly overlapping absorption by free and/or DNA-bound dye (Fig. 1e, f and 6). At all excitation wavelengths, apparent fluorescence emission peaks were observed. However, the peaks were found to be light scattering artefacts because they consistently appeared in parallel control solutions without dye, ever after soaking the fluorescence cuvettes in concentrated sulfuric acid overnight (Fig. S13). The results of these experiments suggest that dye **10** does not engage in a significant degree of DNA intercalation. However, the absence of fluorescence does not necessarily rule out the possibility of J-type aggregation. While DNA-templated cyanine J aggregates generally fluorescence, their emission is highly dependent on dye structure and the local environment.[68] Interactions between cyanine J aggregates and DNA can introduce changes in molecular geometry that accelerate competing non-radiative decay pathways that strongly quench emission.[101,103,107]

3.4.4 Competitive binding analyses. To test for groove binding interactions, the classical groove binders pentamidine and methyl green were used to displace pre-bound dye **10** from B-form duplex DNA (pH 7.0). Pentamidine, a well-studied aromatic diamidine with therapeutic activity against a number of infectious fungi and protozoa, binds deeply within the narrow minor groove of AT-rich DNA sequences, making substantial van der Waals contacts with the groove walls, hydrogen bonding interactions with bases, and distant electrostatic interactions with the negatively charged oxygen atoms in the DNA backbone.[108] Some reported equilibrium dissociation constants (K_D) for pentamidine with AATT rich double stranded DNA range from ~5.55 to 7.69 μM, depending on the analytical method employed (pH 7.0).[109] By comparison, methyl green is a bulky triphenylmethane dye that binds in the wider DNA major groove also with a preference for AT rich sequences.[110] Methyl green interacts with DNA in a semi-external fashion with its positively charged dimethylamino groups in close proximity to the negatively charged phosphate backbone, and its hydrophobic core packed against the exposed base edges in the major groove floor.[111] A reported K_D value of methyl green for B-form DNA is ~11.3 μM (pH 6.9, 50 mM NaCl), which decreases as a function of increasing ionic strength.[112] The respective minor and major groove binders pentamidine[109] and methyl green[113] can effectively complete for binding sites in B-form DNA, directly displacing ligands pre-bound to their individual grooves.

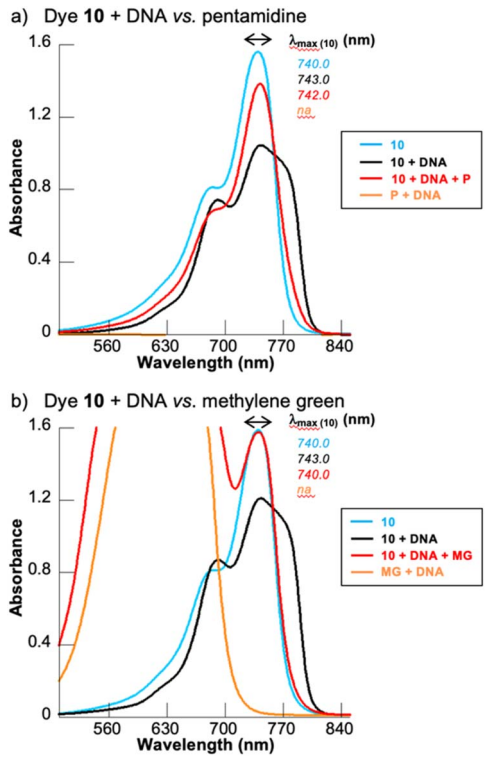

Fig. 8 UV-visible absorption spectra of solutions containing 10 mM sodium phosphate buffer pH 7.0 mixed with combinations of 10 μM of dye **10**, 150 μM bp CT DNA, and (a) 250 μM of pentamidine (P) or (b) 250 μM of methyl green (MG).

To "push" dye **10** off B-form DNA, to samples containing pH 7.0 buffer, we added one or more of the following agents in the order: CT DNA, dye **10**, methyl green or pentamidine. UV-visible absorption spectra of the resulting solutions were then recorded and compared as shown in Fig. 8 and S14. When either competing ligand, methyl green or pentamidine, was added to dye **10**/CT DNA solutions, the dye's spectral absorption band reverted back to a shape very similar to the band generated by free dye in buffer (no DNA; blue lines, Fig. 8), but was markedly different from corresponding band in the UV-visible spectrum of DNA-bound dye (no competitor; black lines, Fig. 8). When DNA was omitted from the prepared solutions, methyl green and pentamidine addition did not significantly change cyanine dye **10**'s main UV-visible band (green *vs.* blue lines in Fig S14). This suggests that the groove binders pentamidine and methyl green are unlikely to "remove" dye **10** from B-form DNA by directly binding to free dye and shifting its equilibrium in solution. Our spectra instead indicate that the competitors eject the dye by binding directly to DNA. A careful look at Fig. 8 shows that major groove binder methyl green is in fact more effective than minor groove binding pentamidine in resorting the 740 nm λ_{max} of the putative monomeric form of free dye **10** and in eliminating the bathochromic shoulder that our CD studies associated with DNA templated J-type aggregation (Fig. 7). Do the competitors displace dye **10** by directly competing for DNA binding sites in their respective grooves or by altering DNA structure? Pentamidine causes only minimal distortions to the B-form helix, which primarily occur in the DNA minor groove.[108,114] Similar to pentamidine,[108,114] the major groove binder methyl green affects only minor DNA structural changes.[111] However unlike pentamidine,[113] methyl green binding to the major groove can initiate cross-talk that can cause weak to moderate levels of displacement of DNA ligands from the opposing minor groove.[115] There are no clear and explicit examples of cyanines that bind to the B-form DNA major groove, only limited, indirect evidence of major groove interactions.[116,117] The shape, size, and hydrophobicity of most monomeric and aggregated cyanine dyes are a much better fit for narrower width of the B-form DNA minor groove.[68] This being considered, our pentamidine results suggest that dye **10** binds directly to the minor groove of DNA. While the efficient displacement of cyanine dye **10** by methyl green could point to direct, major groove interactions, displacement by cross-talk between grooves is indicated by literature precedent.[115–117]

3.5 Antimicrobial photodynamic activity in *E. coli*

We next compared the photodynamic effects of the di-cationic and mono-cationic heptamethine carbocyanine dyes **10** and **9** *vs.* the established aPDT agents[24,32–36] mono-anionic heptamethine carbocyanine indocyanine green and the mono-cationic phenothiazine dye methylene blue, in Gram-negative XL1-Blue K-12 *E. coli* cells.[40] This was done by equilibrating parallel solutions of the dyes at concentrations ranging from 0 to 50 μM in the dark or under 638 nm (MB) or 780 nm (**9**, **10**, ICG) illumination. After spreading the cells on individual LB

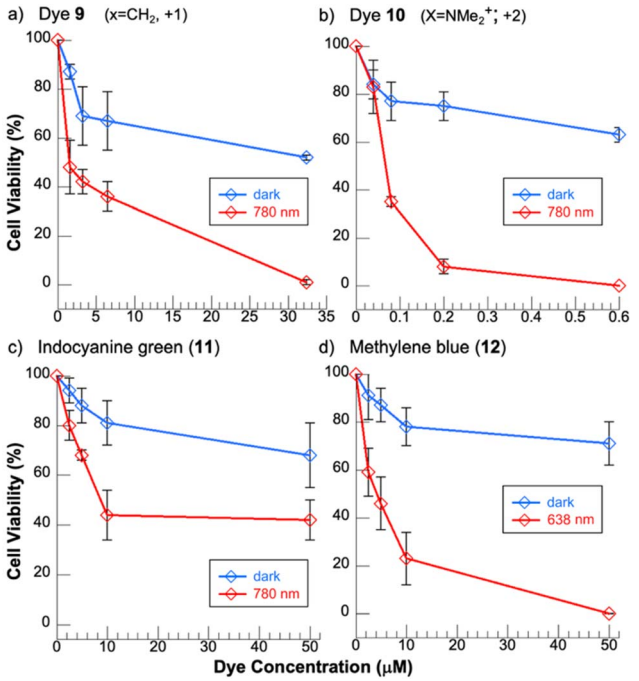

Fig. 9 Final dye concentrations ranging from: (a) 0 to 32 μM of **9**, (b) 0 to 0.6 μM of **10**, (c) 0 to 50 μM of indocyanine green (**11**), and (d) 0 to 50 μM of methylene blue (**12**; Fig S1) were added to aliquots of cultured *E. coli* strain K12 cells in LB broth (40 μL total volume). Each reaction was equilibrated for 5 min, then the cells were either kept in the dark or irradiated for 30 min with: (a–c) a 780 nm, 1.8 W cm^{-2} LED laser or (d) a 638 nm 2.8 W cm^{-2} LED laser (22 °C). Reactions were then spread on LB plates and grown for 16 h at 37 °C in the dark. Colonies were counted using ImageJ software. Each point on the plot represents the average cell viability (%) from 3 independent trials, with error bars indicating standard deviation.

plates and overnight incubation, cell viability percentages were calculated (Fig. 9).

Our results show that all four dyes were more toxic to the bacterial cells when irradiated, with light alone having no effect on cell viability (red *vs.* blue lines). Under 780 nm *hν*, carbocyanine **10** was ~10 times more effective in inhibiting *E. coli* bacterial growth compared to dyes **9**, ICG, and MB (Fig. 9 and S1). Most notably, at 0.20 μM of carbocyanine dye **10**, a total of 8 ± 3% of cells survived under 780 nm NIR illumination compared to 75 ± 6% of dye-treated *E. coli* cells kept in the dark. Compound **10**, a dicationic carbocyanine with terminal fluorinated indolium rings and a central heptamethine bridge with a chlorinated cyclohexene quaternary ammonium group, also shows ~ tenfold greater photodynamic efficacy in eliminating Gram-negative *E. coli* when compared to results reported in the literature for premiere NIR carbocyanine dyes, including those modified with heavy atoms to optimize ROS yields.[47–49] These comparator dyes are mono-[47,49] or dicationic[48] carbocyanines with benzylated 4-quinolinium,[49] benzoselenazole,[47] benzothiazole,[47] or iodinated indolium[48] terminal groups, connected by a pentamethine[49] or heptamethine[47,48] bridge, with[47] or without[48,49] a central chlorinated cyclohexene ring.

4 Conclusions

Antimicrobial photodynamic therapy (aPDT) has emerged as a promising strategy to response to the challenge to global health presented by antibiotic resistant bacteria.[2–4] Upon light activation, aPDT agents generate cytotoxic, short-lived ROS with broad oxidative capabilities[11–14] that suppress the development of drug resistance[4,6,17,18] and demonstrate efficacy against bacterial infections resistant to multiple drugs.[19,20]

With a single quaternary ammonium group (QAC = 1) and an overall charge of +2, carbocyanine **10** demonstrated significantly greater efficacy than mono-cationic dye **9** (QAC = 0) in photosensitizing DNA direct strand breaks, hydroxyl radical and singlet oxygen generation, and Gram-negative bacterial cell death (Fig. 2, 4, and 9). Design elements in common to both dyes include: extended polymethine conjugation to red-shift absorption into the tissue-penetrating NIR wavelength range, and the placement of halogen atoms, chlorine to reduce dye autoxidation[55,56] and to promote intersystem crossing from the singlet to triplet excited dye states,[57] and fluorine to encourage hydrophobic interactions with the phospholipid bilayers present in bacterial cell walls.[61] Taking into consideration that DNA[37] and bacterial cell walls are negatively charged,[38,39] our comparison of carbocyanines **9** and **10** underscores the importance of QAC content and net positive charge to the photodynamic action of antibacterial aPDT agents. We are now incorporating new quaternary ammonium design elements into next-generation NIR cyanine-based photosensitizers for antimicrobial applications.

Author contributions

Carine P. Seudieu Seudieu: investigation, methodology, data curation, writing – original draft; Güliz Ersoy Özmen: methodology, data curation, writing – review & editing; Imran Khan: methodology, data curation, writing – review & editing; Maged Henary: conceptualization, supervision, project administration, writing – review & editing; Kathryn B. Grant: conceptualization, formal analysis, supervision, project administration, writing – original draft.

Conflicts of interest

There are no conflicts to declare.

Data availability

The data supporting this article have been included as supplementary information (SI). Supplementary information: Fig. S1 to S14 and further experimental details. See DOI: https://doi.org/10.1039/d6ra01566b.

Acknowledgements

Maged Henary acknowledges funding from National Institutes of Health (Grants R01EB034731 and R01CA280968B).

Notes and references

1 E. Sanchez and S. Doron, *Bacterial Infections: Overview, International Encyclopedia of Public Health*, vol 1, 2nd edn, 2017, pp. 196–205.

2 F. P. Sellera, C. P. Sabino, S. C. Nunez and M. S. Ribeiro, Clinical acceptance of antimicrobial photodynamic therapy in the age of WHO global priority pathogens: So what we need to move forward?, *Photodiagnosis Photodyn. Ther.*, 2022, **40**, 103158.

3 C. J. L. Murray, K. S. Ikuta, F. Sharara, L. Swetschinski, G. R. Aguilar, A. Gray, C. Han, C. Bisignano, P. Rao, E. Wool, S. C. Johnson, A. J. Browne, M. G. Chipeta, F. Fell, S. Hackett, G. Haines-Woodhouse, B. H. K. Hamadani, E. A. P. Kumaran, B. McManigal, R. Agarwal, S. Akech, S. Albertson, J. Amuasi, J. Andrews, A. Aravkin, E. Ashley, F. Bailey, S. Baker, B. Basnyat, A. Bekker, R. Bender, A. Bethou, J. Bielicki, S. Boonkasidecha, J. Bukosia, C. Carvalheiro, C. Castañeda-Orjuela, V. Chansamouth, S. Chaurasia, S. Chiurchiù, F. Chowdhury, A. J. Cook, B. Cooper, T. R. Cressey, E. Criollo-Mora, M. Cunningham, S. Darboe, N. P. J. Day, M. De Luca, K. Dokova, A. Dramowski, S. J. Dunachie, T. Eckmanns, D. Eibach, A. Emami, N. Feasey, N. Fisher-Pearson, K. Forrest, D. Garrett, P. Gastmeier, A. Z. Giref, R. C. Greer, V. Gupta, S. Haller, A. Haselbeck, S. Hay, M. Holm, S. Hopkins, K. C. Iregbu, J. Jacobs, D. Jarovsky, F. Javanmardi, M. Khorana, N. Kissoon, E. Kobeissi, T. Kostyanev, F. Krapp, R. Krumkamp, A. Kumar, H. H. Kyu, C. Lim, D. Limmathurotsakul, M. J. Loftus, M. Lunn, J. Ma, N. Mturi, T. Munera-Huertas, P. Musicha, M. M. Mussi-Pinhata, T. Nakamura, R. Nanavati, S. Nangia, P. Newton, C. Ngoun, A. Novotney, D. Nwakanma, C. W. Obiero, A. Olivas-Martinez, P. Olliaro, E. Ooko, E. Ortiz-Brizuela, A. Y. Peleg, C. Perrone, N. Plakkal, A. Ponce-de-Leon, M. Raad, T. Ramdin, A. Riddell, T. Roberts, J. VictoriaRobotham, A. Roca, K. E. Rudd, N. Russell, J. Schnall, J. A. G. Scott, M. Shivamallappa, J. Sifuentes-Osornio, N. Steenkeste, A. J. Stewardson, T. Stoeva, N. Tasak, A. Thaiprakong, G. Thwaites, C. Turner, P. Turner, H. R. van Doorn, S. Velaphi, A. Vongpradith, H. Vu, T. Walsh, S. Waner, T. Wangrangsimakul, T. Wozniak, P. Zheng, B. Sartorius, A. D. Lopez, A. Stergachis, C. Moore, C. Dolecek, M. Naghavi and A. R. Collabora, Global burden of bacterial antimicrobial resistance in 2019: A systematic analysis, *Lancet*, 2022, **399**, 629–655.

4 M. Almenara-Blasco, V. Pérez-Laguna, A. Navarro-Bielsa, T. Gracia-Cazaña and Y. Gilaberte, Antimicrobial photodynamic therapy for dermatological infections: Current insights and future prospects, *Front. Photobiol.*, 2024, **2**, 1–14.

5 T. J. Beveridge, Structures of gram-negative cell walls and their derived membrane vesicles, *J. Bacteriol.*, 1999, **181**, 4725–4733.

6 F. Akhtar, L. Misba and A. U. Khan, The dual role of photodynamic therapy to treat cancer and microbial infection, *Drug Discov. Today*, 2024, **29**, 104099.

7 Z. Y. Li and K. B. Grant, DNA photo-cleaving agents in the far-red to near-infrared range – A review, *RSC Adv.*, 2016, **6**, 24617–24634.

8 L. X. Lv, B. L. Fan, X. R. Ji, Y. X. Liu, T. Chen, Y. L. Li, X. Y. Gao, P. Chen, B. Tang and G. Chen, From the clinical perspective of photodynamic therapy and photothermal therapy: Structure-activity-practice, *Coordin. Chem. Rev.*, 2024, **507**, 215733.

9 R. G. Zepp, B. C. Faust and J. Hoigne, Hydroxyl radical formation in aqueous reactions (pH 3–8) of iron(II) with hydrogen-peroxide - the photo-Fenton reaction, *Environ. Sci. Technol.*, 1992, **26**, 313–319.

10 E. F. Silva, C. Serpa, J. M. Dabrowski, C. J. Monteiro, S. J. Formosinho, G. Stochel, K. Urbanska, S. Simoes, M. M. Pereira and L. G. Arnaut, Mechanisms of singlet-oxygen and superoxide-ion generation by porphyrins and bacteriochlorins and their implications in photodynamic therapy, *Chemistry*, 2010, **16**, 9273–9286.

11 G. M. Makrigiorgos, Detection of chromatin-associated hydroxyl radicals generated by DNA-bound metal compounds and antitumor antibiotics, *Met. Ions Biol. Syst.*, 1999, **36**, 521–545.

12 S. Hatz, L. Poulsen and P. R. Ogilby, Time-resolved singlet oxygen phosphorescence measurements from photosensitized experiments in single cells: effects of oxygen diffusion and oxygen concentration, *Photochem. Photobiol.*, 2008, **84**, 1284–1290.

13 H. Sies, Strategies of antioxidant defense, *Eur. J. Biochem.*, 1993, **215**, 213–219.

14 S. Hatz, J. D. C. Lambert and P. R. Ogilby, Measuring the lifetime of singlet oxygen in a single cell: addressing the issue of cell viability, *Photoch. Photobio. Sci.*, 2007, **6**, 1106–1116.

15 T. Mishchenko, I. Balalaeva, A. Gorokhova, M. Vedunova and D. V. Krysko, Which cell death modality wins the contest for photodynamic therapy of cancer?, *Cell Death Dis.*, 2022, **13**, 455.

16 M. A. Triana, Y. F. Feng, S. J. Saiji, Y. T. Tang, R. J. Lanzafame, N. K. Eidenschink, S. Khan, Y. J. Dong and T. Hasan, Advancing flexible quantum dot light-emitting diode technology for antimicrobial photodynamic therapy, *npj Flex. Electron.*, 2025, **9**, 1–13.

17 L. Gholami, S. Shahabi, M. Jazaeri, M. Hadilou and R. Fekrazad, Clinical applications of antimicrobial photodynamic therapy in dentistry, *Front. Microbiol.*, 2023, **13**, 1–47.

18 G. Z. Wu, Z. Xu, Y. Yu, M. L. Zhang, S. S. Wang, S. Duan and X. L. Liu, Biomaterials-based phototherapy for bacterial infections, *Front. Pharmacol*, 2024, **15**, 1513850.

19 W. Z. Liu, Y. X. Zhang, W. W. You, J. Q. Su, S. H. Yu, T. Dai, Y. M. Huang, X. Y. Chen, X. R. Song and Z. Chen, Near-infrared-excited upconversion photodynamic therapy of extensively drug-resistant *Acinetobacter baumannii* based

on lanthanide nanoparticles, *Nanoscale*, 2020, **12**, 13948–13957.

20 R. R. Sarker, Y. Tsunoi, Y. Haruyama, S. Sato and I. Nishidate, Depth distributions of bacteria for the infected burn wounds treated by methylene blue-mediated photodynamic therapy in rats: effects of additives to photosensitizer, *J. Biomed. Opt.*, 2022, **27**, 1–12.

21 R. D. Rodrigues, N. S. Araujo, J. M. Pinto, C. L. Z. Vieira, D. A. Ribeiro, J. N. dos Santos and P. R. Cury, Photodynamic therapy as adjunctive treatment of single-rooted teeth in patients with grade C periodontitis: A randomized controlled clinical trial, *Photodiagn. Photodyn.*, 2023, **44**, 103776.

22 M. N. Alasqah, Efficacy of methylene blue-mediated antimicrobial photodynamic therapy on clinical and radiographic outcomes among patients with periodontal diseases: A systematic review and meta-analysis of randomized controlled trials, *Photodiagn. Photodyn.*, 2024, **46**, 104000.

23 P. O. Cunha, I. R. Gonsales, S. L. A. Greghi, A. C. P. Sant'ana, H. M. Honorio, C. A. Negrato, M. S. R. Zangrando and C. A. Damante, Adjuvant antimicrobial photodynamic therapy improves periodontal health and reduces inflammatory cytokines in patients with type 1 diabetes mellitus, *J. Appl. Oral Sci.*, 2024, **32**, e20240258.

24 E. Dube, Antimicrobial photodynamic therapy: Self-disinfecting surfaces for controlling microbial infections, *Microorganisms*, 2024, **12**, 1573.

25 J. G. Jiang, X. Y. Lv, H. J. Cheng, D. L. Yang, W. J. Xu, Y. L. Hu, Y. N. Song and G. S. Zeng, Type I photodynamic antimicrobial therapy: Principles, progress, and future perspectives, *Acta Biomater.*, 2024, **177**, 1–19.

26 M. K. K. Perumal, R. R. Renuka and P. M. Natarajan, Evaluating the potency of laser-activated antimicrobial photodynamic therapy utilizing methylene blue as a treatment approach for chronic periodontitis, *Front. Oral Health*, 2024, **5**, 1407201.

27 M. M. Al-Momani, Indocyanine-mediated antimicrobial photodynamic therapy promotes superior clinical effects in stage III and grade C chronic periodontitis among controlled and uncontrolled diabetes mellitus: A randomized controlled clinical trial, *Photodiagn. Photodyn.*, 2021, **35**, 102379.

28 S. Brinar, A. Skvarca, B. Gaspirc and R. Schara, The effect of antimicrobial photodynamic therapy on periodontal disease and glycemic control in patients with type 2 diabetes mellitus, *Clin. Oral Invest.*, 2023, **27**, 6235–6244.

29 R. D. Leonardo, C. G. Puente, F. L. C. V. Berbert, G. Faria, C. K. Nishiyama, F. A. Orosco, G. W. L. Rodrigues, A. P. F. Ribeiro, L. T. A. Cintra and M. Trope, Clinical study of antimicrobial efficacy of laser ablation therapy with indocyanine green in root canal treatment, *J. Endodont.*, 2023, **49**, 990–994.

30 D. O. Cetiner, S. C. Isler, R. Ilikci-Sagkan, J. Sengul, O. Kaymaz and A. U. Corekci, The adjunctive use of antimicrobial photodynamic therapy, light-emitting-diode photobiomodulation and ozone therapy in regenerative treatment of stage III/IV grade C periodontitis: a randomized controlled clinical trial, *Clin. Oral Investig.*, 2024, **28**, 426.

31 J. Hayashi, K. Ono, Y. Iwamura, Y. Sasaki, T. Ohno, R. Goto, E. Nishida, G. Yamamoto, T. Kikuchi, N. Higuchi, A. Mitani and M. Fukuda, Suppression of subgingival bacteria by antimicrobial photodynamic therapy using transgingival irradiation: A randomized clinical trial, *J. Periodontol.*, 2024, **95**, 718–728.

32 S. Bouillaguet, J. C. Wataha, O. Zapata, M. Campo, N. Lange and J. Schrenzel, Production of reactive oxygen species from photosensitizers activated with visible light sources available in dental offices, *Photomed. Laser Surg*, 2010, **28**, 519–525.

33 K. Quinlan, A patented medical home-use device that treats and prevents oral diseases, *Brit. Dent. J.*, 2023, **235**, 825.

34 E. Dolinska, A. Skurska, M. Pietruska, V. Dymicka-Piekarska, R. Milewski and A. Sculean, Effect of nonsurgical periodontal therapy with additional photodynamic therapy on the level of MMP-9 and TIMP-1 in GCF in chronic periodontitis patients-a preliminary pilot study, *Adv. Med. Sci.*, 2024, **69**, 362–367.

35 A. Maj, A. Kusiak, K. Garbacz, D. Cichonska and D. Swietlik, Photodynamic therapy in non-surgical treatment of periodontitis, *Sci. Rep.*, 2025, **15**, 5903.

36 L. Pires, B. C. Wilson, R. Bremner, A. Lang, J. Larouche, R. McDonald, J. D. Pearson, D. Trcka, J. Wrana, J. Wu and C. M. Whyne, Translational feasibility and efficacy of nasal photodynamic disinfection of SARS-CoV-2, *Sci. Rep.*, 2022, **12**, 14438.

37 A. A. Zinchenko, V. G. Sergeyev, K. Yamabe, S. Murata and K. Yoshikawa, DNA compaction by divalent cations: Structural specificity revealed by the potentiality of designed quaternary diammonium salts, *ChemBioChem*, 2004, **5**, 360–368.

38 M. C. Jennings, K. P. C. Minbiole and W. M. Wuest, Quaternary ammonium compounds: An antimicrobial mainstay and platform for innovation to address bacterial resistance, *ACS Infect. Dis.*, 2015, **1**, 288–303.

39 Y. Jiao, L. N. Niu, S. Ma, J. Li, F. R. Tay and J. H. Chen, Quaternary ammonium-based biomedical materials: State-of-the-art, toxicological aspects and antimicrobial resistance, *Prog. Polym. Sci.*, 2017, **71**, 53–90.

40 S. Achatz and A. Skerra, Comparative genome analysis of three classical E. coli cloning strains designed for blue/white selection: JM83, JM109 and XL1-Blue, *FEBS Open Bio*, 2024, **14**, 888–905.

41 J. Sambrook, E. F. Fritsch, and T. Miniatis, *Molecular Cloning: A Laboratory Manual Cold Springs Harbor Laboratory Press*, Cold Springs Harbor, NY, 2nd edn, 1989.

42 R. P. Hertzberg and P. B. Dervan, Cleavage of double helical DNA by (methidiumpropyl-EDTA)-iron(II), *J. Am. Chem. Soc.*, 1982, **104**, 313–315.

43 I. Johnson and M. Spence, in *The Molecular Probes Handbook: A Guide to Fluorescent Probes and Labeling Technologies*, ed. I. Johnson and M. Spence, Life Technologies Corporation, 11 edn, 2010, Chapter 18.

44 C. Flors, M. J. Fryer, J. Waring, B. Reeder, U. Bechtold, P. M. Mullineaux, S. Nonell, M. T. Wilson and N. R. Baker, Imaging the production of singlet oxygen using a new fluorescent sensor, Singlet Oxygen Sensor Green®, *J. Exp. Bot.*, 2006, **57**, 1725–1734.

45 M. Price, J. J. Reiners, A. M. Santiago and D. Kessel, Monitoring singlet oxygen and hydroxyl radical formation with fluorescent probes during photodynamic therapy, *Photochem. Photobiol.*, 2009, **85**, 1177–1181.

46 J. Yuan, H. Yang, W. Huang, S. Liu, H. Zhang, X. Zhang and X. Peng, Design strategies and applications of cyanine dyes in phototherapy, *Chem. Soc. Rev.*, 2025, **54**, 341–366.

47 A. V. Prakash, F. Yazabak, I. Hovor, F. Nakonechny, O. Kulyk, O. Semenova, A. Bazylevich, G. Gellerman and L. Patsenker, Highly efficient near-IR cyclohexene cyanine photosensitizers for antibacterial photodynamic therapy, *Dyes Pigments*, 2023, **211**, 1–10.

48 O. Semenova, D. Kobzev, I. Hovor, M. Atrash, F. Nakonechny, O. Kulyk, A. Bazylevich, G. Gellerman and L. Patsenker, Effect of solubilizing group on the antibacterial activity of heptamethine cyanine photosensitizers, *Pharmaceutics*, 2023, **15**, 1–20.

49 E. O. Ahoulou, A. Ugboya, V. Ogbonna, K. Basnet, M. Henary and K. B. Grant, Single-photon DNA photocleavage up to 905 nm by a benzylated 4-quinolinium carbocyanine dye, *ACS Omega*, 2025, **10**, 6544–6558.

50 N. Sellet, J. Frey, M. Cormier and J. P. Goddard, Near-infrared photocatalysis with cyanines: Synthesis, applications and perspectives, *Chem. Sci.*, 2024, **15**, 8639–8650.

51 Z. Mahmut, C. Zhang, F. Ruan, N. Shi, X. Zhang, Y. Wang, X. Zheng, Z. Tang, B. Dong, D. Gao and J. Sun, Medical applications and advancement of near infrared photosensitive indocyanine green molecules, *Molecules*, 2023, **28**, 1–30.

52 D. H. Li, C. L. Schreiber and B. D. Smith, Sterically shielded heptamethine cyanine dyes for bioconjugation and high performance near-infrared fluorescence imaging, *Angew. Chem., Int. Ed.*, 2020, **59**, 12154–12161.

53 J. C. Kihn, C. L. Masy and M. M. Mestdagh, Yeast flocculation: competition between nonspecific repulsion and specific bonding in cell adhesion, *Can. J. Microbiol.*, 1988, **34**, 773–778.

54 H. Ebrahimi, F. Siavoshi, M. H. Jazayeri, A. Sarrafnejad, P. Saniee and M. Mobini, Physicochemical properties of intact fungal cell wall determine vesicles release and nanoparticles internalization, *Heliyon*, 2023, **9**, 1–10.

55 T. C. Barros, S. H. Toma, H. E. Toma, E. L. Bastos and M. S. Baptista, Polymethine cyanine dyes in beta-cyclodextrin solution: multiple equilibria and chemical oxidation, *J. Phys. Org. Chem.*, 2010, **23**, 893–903.

56 D. Oushiki, H. Kojima, T. Terai, M. Arita, K. Hanaoka, Y. Urano and T. Nagano, Development and application of a near-Infrared fluorescence probe for oxidative stress based on differential reactivity of linked cyanine dyes, *J. Am. Chem. Soc.*, 2010, **132**, 2795–2801.

57 A. Gorman, J. Killoran, C. O'Shea, T. Kenna, W. M. Gallagher and D. F. O'Shea, *In vitro* demonstration of the heavy-atom effect for photodynamic therapy, *J. Am. Chem. Soc.*, 2004, **126**, 10619–10631.

58 I. E. Borissevitch, P. J. Gonçalves, L. P. Ferreira, A. A. Kostyukov and V. A. Kuzmin, Characterization of triplet state of cyanine dyes with two chromophores effect of molecule structure, *Technologies*, 2023, **11**, 1–12.

59 H. J. Böhm, D. Banner, S. Bendels, M. Kansy, B. Kuhn, K. Müller, U. Obst-Sander and M. Stahl, Fluorine in medicinal chemistry, *ChemBioBhem*, 2004, **5**, 637–643.

60 C. D. Murphy and G. Sandford, Recent advances in fluorination techniques and their anticipated impact on drug metabolism and toxicity, *Expert Opin. Drug Met. Tox.*, 2015, **11**, 589–599.

61 S. Bhatt and S. Chatterjee, Fluoroquinolone antibiotics: Occurrence, mode of action, resistance, environmental detection, and remediation-A comprehensive review, *Environ. Pollut.*, 2022, **315**, 1–14.

62 Y. W. Jiang, W. X. Lin, S. B. Tan, Y. X. Wang, W. Wu and Z. G. Lu, Synthesis and antibacterial evaluation of novel vancomycin derivatives containing quaternary ammonium moieties, *ACS Omega*, 2023, **8**, 28511–28518.

63 C. Gao, R. R. Li, Y. B. Li, Y. Q. Wu, Y. Qu, M. Ampomah-Wireko, J. B. Zheng, Z. Y. Wang, Y. N. Wang and E. Zhang, Design, synthesis and evaluation of quinolone quaternary ammonium antibacterial agent with killing ability to biofilm, *Bioorg. Chem.*, 2025, **162**, 1–16.

64 P. Verma and H. Pal, Aggregation studies of dipolar coumarin-153 dye in polar solvents: A photophysical study, *J. Phys. Chem. A*, 2014, **118**, 6950–6964.

65 S. Bataju and N. Pantha, Hydrophobicity of an isobutane dimer in water, methanol and acetonitrile as solvents – A classical molecular dynamics study, *Int. J. Mod. Phys. B*, 2019, **33**, 1950391.

66 G. Beckford, E. Owens, M. Henary and G. Patonay, The solvatochromic effects of side chain substitution on the binding interaction of novel tricarbocyanine dyes with human serum albumin, *Talanta*, 2012, **92**, 45–52.

67 K. Basnet, T. Fatemipouya, A. St Lorenz, M. Nguyen, O. Taratula, M. Henary and K. B. Grant, Single photon DNA photocleavage at 830 nm by quinoline dicarbocyanine dyes, *Chem. Commun.*, 2019, **55**, 12667–12670.

68 B. A. Armitage, in *DNA Binders and Related Subjects*, ed. M. Waring and J. Chaires, Springer Berlin Heidelberg, 2005, vol. 253, ch. 3, pp. 55–76.

69 B. Le Guennic and D. Jacquemin, Taking up the cyanine challenge with quantum tools, *Accounts Chem. Res.*, 2015, **48**, 530–537.

70 J. L. Seifert, R. E. Connor, S. A. Kushon, M. Wang and B. A. Armitage, Spontaneous assembly of helical cyanine dye aggregates on DNA nanotemplates, *J. Am. Chem. Soc.*, 1999, **121**, 2987–2995.

71 M. M. Wang, G. L. Silva and B. A. Armitage, DNA-templated formation of a helical cyanine dye J-aggregate, *J. Am. Chem. Soc.*, 2000, **122**, 9977–9986.

72 M. A. Kohanski, D. J. Dwyer, B. Hayete, C. A. Lawrence and J. J. Collins, A common mechanism of cellular death induced by bactericidal antibiotics, *Cell*, 2007, **130**, 797–810.

73 J. J. Foti, B. Devadoss, J. A. Winkler, J. J. Collins and G. C. Walker, Oxidation of the guanine nucleotide pool underlies cell death by bactericidal antibiotics, *Science*, 2012, **336**, 315–319.

74 D. Y. Ye, J. Sun, R. Jiang, J. S. Chang, Y. M. Liu, X. Z. Wu, L. Q. Li, Y. H. Luo, J. Wang, K. K. Guo and Z. Q. Yang, β-lactam antibiotics induce metabolic perturbations linked to ROS generation leads to bacterial impairment, *Front. Microbiol.*, 2024, **15**, 1–14.

75 Y. Y. Liu and J. A. Imlay, Cell death from antibiotics without the involvement of reactive oxygen species, *Science*, 2013, **339**, 1210–1213.

76 R. Brem, M. Guven and P. Karran, Oxidatively-generated damage to DNA and proteins mediated by photosensitized UVA, *Free Radical Bio. Med.*, 2017, **107**, 101–109.

77 C. T. Mapp, E. A. Owens, M. Henary and K. B. Grant, Oxidative cleavage of DNA by pentamethine carbocyanine dyes irradiated with long-wavelength visible light, *Bioorg. Med. Chem. Lett.*, 2014, **24**, 214–219.

78 E. O. Ahoulou, K. K. Drinkard, K. Basnet, A. St Lorenz, O. Taratula, M. Henary and K. B. Grant, DNA photocleavage in the near-infrared wavelength range by 2-quinolinium dicarbocyanine dyes, *Molecules*, 2020, **25**, 1–17.

79 B. Akerman and E. Tuite, Single- and double-strand photocleavage of DNA by YO, YOYO and TOTO, *Nucleic Acids Res.*, 1996, **24**, 1080–1090.

80 K. Keyer, A. S. Gort and J. A. Imlay, Superoxide and the production of oxidative DNA-damage, *J. Bacteriol.*, 1995, **177**, 6782–6790.

81 K. Jomova, R. Raptova, S. Y. Alomar, S. H. Alwasel, E. Nepovimova, K. Kuca and M. Valko, Reactive oxygen species, toxicity, oxidative stress, and antioxidants: chronic diseases and aging, *Arch. Toxicol.*, 2023, **97**, 2499–2574.

82 J. M. Gutteridge, Ferrous-salt-promoted damage to deoxyribose and benzoate. The increased effectiveness of hydroxyl-radical scavengers in the presence of EDTA, *Biochem. J.*, 1987, **243**, 709–714.

83 P. B. Merkel and D. R. Kearns, Radiationless decay of singlet molecular oxygen in solution. Experimental and theoretical study of electronic-to-vibrational energy transfer, *J. Am. Chem. Soc.*, 1972, **94**, 7244–7253.

84 F. A. Taiwo, Mechanism of tiron as scavenger of superoxide ions and free electrons, *Spectrosc. Int. J.*, 2008, **22**, 491–498.

85 W. K. Pogozelski and T. D. Tullius, Oxidative strand scission of nucleic acids: routes initiated by hydrogen abstraction from the sugar moiety, *Chem. Rev.*, 1998, **98**, 1089–1108.

86 C. J. Burrows and J. G. Muller, Oxidative nucleobase modifications leading to strand scission, *Chem. Rev.*, 1998, **98**, 1109–1152.

87 A. Ray, K. Liosi, S. N. Ramakrishna, N. D. Spencer, A. Kuzuya and Y. Yamakoshi, Single-molecule AFM study of DNA damage by $^1O_2$ generated from photoexcited C_{60}, *J. Phys. Chem. Lett.*, 2020, **11**, 7819–7826.

88 A. Jana, S. Sahoo, S. Paul, S. Sahoo, C. Jayabaskaran and A. R. Chakravarty, Photodynamic therapy with targeted release of boron-dipyrromethene dye from cobalt(III) prodrugs in red light, *Inorg. Chem.*, 2024, **63**, 6822–6835.

89 D. Mangal, D. Vudathala, J. H. Park, S. H. Lee, T. M. Penning and I. A. Blair, Analysis of 7,8-dihydro-8-oxo-2′-deoxyguanosine in cellular DNA during oxidative stress, *Chem. Res. Toxicol.*, 2009, **22**, 788–797.

90 S. B. Adeloju and A. M. Bond, Influence of laboratory environment on the precision and accuracy of trace element analysis, *Anal. Chem.*, 1985, **57**, 1728–1733.

91 M. Gasparon, Trace metals in water samples: minimising contamination during sampling and storage, *Environ. Geol.*, 1998, **36**, 207–214.

92 M. Chevion, Y. D. Jiang, R. Harel, E. Berenshtein, G. Uretzky and N. Kitrossky, Copper and Iron Are Mobilized Following Myocardial-Ischemia - Possible Predictive Criteria for Tissue-Injury, *Proc. Natl. Acad. Sci. U. S. A.*, 1993, **90**, 1102–1106.

93 H. Z. Bai, M. Wu, H. J. Zhang and G. P. Tang, Chronic polycyclic aromatic hydrocarbon exposure causes DNA damage and genomic instability in lung epithelial cells, *Oncotarget*, 2017, **8**, 79034–79045.

94 Y. Yu, Y. Yan, F. L. Niu, Y. J. Wang, X. Y. Chen, G. D. Su, Y. R. Liu, X. L. Zhao, L. Qian, P. Liu and Y. Y. Xiong, Ferroptosis: a cell death connecting oxidative stress, inflammation and cardiovascular diseases, *Cell Death Discov.*, 2021, **7**, 193.

95 Y. Li, Y. H. Du, Y. Zhou, Q. H. Chen, Z. J. Luo, Y. F. Ren, X. D. Chen and G. A. Chen, Iron and copper: Critical executioners of ferroptosis, cuproptosis and other forms of cell death, *Cell Commun. Signal.*, 2023, **21**, 327.

96 E. O. Olufunmilayo, M. B. Gerke-Duncan and R. M. D. Holsinger, Oxidative stress and antioxidants in neurodegenerative disorders, *Antioxidants*, 2023, **12**(2), 517.

97 A. G. Kozlov, R. Galletto and T. M. Lohman, SSB-DNA binding monitored by fluorescence intensity and anisotropy, *Methods Mol. Biol.*, 2012, **922**, 55–83.

98 M. Eriksson and B. Nordén, Linear and circular dichroism of drug-nucleic acid complexes, *Method. Enzymol.*, 2001, **340**, 68–98.

99 J. T. Petty, J. A. Bordelon and M. E. Robertson, Thermodynamic characterization of the association of cyanine dyes with DNA, *J. Phys. Chem. B*, 2000, **104**, 7221–7227.

100 L. I. Markova, V. L. Malinovskii, L. D. Patsenker and R. Häner, J- *vs.* H-type assembly: pentamethine cyanine (Cy5) as a near-IR chiroptical reporter, *Chem. Commun.*, 2013, **49**, 5298–5300.

101 B. L. Cannon, L. K. Patten, D. L. Kellis, P. H. Davis, J. Lee, E. Graugnard, B. Yurke and W. B. Knowlton, Large Davydov splitting and strong fluorescence suppression: An investigation of exciton delocalization in DNA-

templated Holliday Junction dye aggregates, *J. Phys. Chem. A*, 2018, **122**, 2086–2095.

102 M. Chiriboga, S. A. Diaz, D. Mathur, D. A. Hastman, J. S. Melinger, R. Veneziano and I. L. Medintz, Understanding self-assembled pseudoisocyanine dye aggregates in DNA nanostructures and their exciton relay transfer capabilities, *J. Phys. Chem. B*, 2022, **126**, 110–122.

103 M. Chiriboga, C. M. Green, D. Mathur, D. A. Hastman, J. S. Melinger, R. Veneziano, I. L. Medintz and S. A. Díaz, Structural and optical variation of pseudoisocyanine aggregates nucleated on DNA substrates, *Methods Appl. Fluoresc.*, 2023, **11**, 014003.

104 N. S. S. Nizar, M. Sujith, K. Swathi, C. Sissa, A. Painelli and K. G. Thomas, Emergent chiroptical properties in supramolecular and plasmonic assemblies, *Chem. Soc. Rev.*, 2021, **50**, 11208–11226.

105 H. J. Karlsson, M. Eriksson, E. Perzon, B. Åkerman, P. Lincoln and G. Westman, Groove-binding unsymmetrical cyanine dyes for staining of DNA: syntheses and characterization of the DNA-binding, *Nucleic Acids Res.*, 2003, **31**, 6227–6234.

106 M. J. Ruedas-Rama, A. Orte, M. C. Martin-Domingo, F. Castello, E. M. Talavera and J. M. Alvarez-Pez, Interaction of YOYO-3 with different DNA templates to form H-aggregates, *J. Phys. Chem. B*, 2014, **118**, 6098–6106.

107 J. S. Huff, P. H. Davis, A. Christy, D. L. Kellis, N. Kandadai, Z. S. D. Toa, G. D. Scholes, B. Yurke, W. B. Knowlton and R. D. Pensack, DNA-templated aggregates of strongly coupled cyanine dyes: Nonradiative decay governs exciton lifetimes, *J. Phys. Chem. Lett.*, 2019, **10**, 2386–2392.

108 K. J. Edwards, T. C. Jenkins and S. Neidle, Crystal-structure of a pentamidine oligonucleotide complex - implications for DNA-binding properties, *Biochemistry*, 1992, **31**, 7104–7109.

109 N. N. Degtyareva, B. D. Wallace, A. R. Bryant, K. M. Loo and J. T. Petty, Hydration changes accompanying the binding of minor groove ligands with DNA, *Biophys. J.*, 2007, **92**, 959–965.

110 K. R. Fox, S. L. Higson and J. E. Scott, Methyl green and its analogs bind selectively to AT-rich regions of native DNA, *Eur. J. Histochem.*, 1992, **36**, 263–270.

111 B. Norden, F. Tjerneld and E. Palm, Linear dichroism studies of binding site structures in solution. Complexes between DNA and basic arylmethane dyes, *Biophys. Chem.*, 1978, **8**, 1–15.

112 J. L. Liu, J. H. Li and S. J. Dong, Interaction of brilliant cresyl blue and methylene green with DNA studied by spectrophotometric and voltammetric methods, *Electroanalysis*, 1996, **8**, 803–807.

113 H. U. Schmitz and W. Hubner, Comparative-study of berenil-poly-nucleotide and pentamidine-poly-nucleotide complexes using UV/vis and FTIR spectroscopy, *Biospectroscopy*, 1995, **1**, 275–289.

114 T. C. Jenkins and A. N. Lane, AT selectivity and DNA minor groove binding: Modelling, NMR and structural studies of the interactions of propamidine and pentamidine with $d(CGCGAATTCGCG)_{(2)}$, *BBA-Gene Struct. Expr.*, 1997, **1350**, 189–204.

115 E. Tuite, U. Sehlstedt, P. Hagmar, B. Norden and M. Takahashi, Effects of minor and major groove-binding drugs and intercalators on the DNA association of minor groove-binding proteins RecA and deoxyribonuclease I detected by flow linear dichroism, *Eur. J. Biochem.*, 1997, **243**, 482–492.

116 M. Eriksson, F. Westerlund, M. Mehmedovic, P. Lincoln, G. Westman, A. Larsson and B. Åkerman, Comparing mono- and divalent DNA groove binding cyanine dyes: Binding geometries, dissociation rates, and fluorescence properties, *Biophys. Chem.*, 2006, **122**, 195–205.

117 O. Zhytniakivska, U. Tarabara, P. Kuznietsov, K. Vus, V. Trusova and G. Gorbenko, Molecular docking study of the interactions between cyanine dyes and DNA, *E. Eur. J. Phys.*, 2023, 335–340.